3. On the origin and processes controlling the elemental and isotopic composition of carbonates in hypersaline Andean lakes

Paula A. Vignoni[1,2], Hana Jurikova[2,3], Birgit Schröder[2], Rik Tjallingii[2], Francisco E. Córdoba[4,5], Karina L. Lecomte[6], Sylvia Pinkerneil[2], Ieva Grudzinska[7,8], Anja M. Schleicher[9], Sofía A. Viotto[1], Carla D. Santamans[4,5], James W. B. Rae[3], Achim Brauer[1,2]

[1]Institute of Geosciences, University of Potsdam, Potsdam, Germany
[2]Section Climate Dynamics and Landscape Evolution, GFZ German Research Centre for Geosciences, Potsdam, Germany
[3]School of Earth and Environmental Sciences, University of St Andrews, United Kingdom
[4]Instituto de Ecorregiones Andinas (INECOA), CONICET – Universidad Nacional de Jujuy, Jujuy, Argentina
[5]Instituto de Geología y Minería, Universidad Nacional de Jujuy, Jujuy, Argentina.
[6]Facultad de Ciencias Exactas, Físicas y Naturales, Universidad Nacional de Córdoba – Centro de Investigaciones en Ciencias de la Tierra (CICTERRA), CONICET, Córdoba, Argentina
[7]Geoecology group, Department of Environmental Sciences, University of Basel, Basel, Switzerland
[8]Institute of Biology, University of Latvia, Riga, Latvia
[9]Section Inorganic and Isotope Geochemistry, GFZ German Research Centre for Geosciences, Potsdam, Germany

Geochimica et Cosmochimica Acta 366 (2024) 65–83, https://doi.org/10.1016/j.gca.2023.11.032

Abstract

The Altiplano-Puna Plateau of the Central Andes hosts numerous lakes, playa-lakes, and salars with a great di-versity and abundance of carbonates forming under extreme climatic, hydrologic, and environmental conditions. To unravel the underlying processes controlling the formation of carbonates and their geochemical signatures in hypersaline systems, we investigated coupled brine-carbonate samples in a high-altitude Andean lake using a wide suite of petrographic (SEM, XRD) and geochemical tools ($\delta^{2}H$, $\delta^{18}O$, $\delta^{13}C$, $\delta^{11}B$, major and minor ion composition, aqueous modelling). Our findings show that the inflow of hydrothermal springs in combination with strong CO_2 degassing and evaporation plays an important role in creating a spatial diversity of hydro- chemical sub-environments allowing different types of microbialites (microbial mounds and mats), travertines, and fine-grained calcite minerals to form. Carbonate precipitation occurs in hot springs triggered by a shift in carbonate equilibrium by hydrothermal CO2 degassing and microbially-driven elevation of local pH at crystal-lisation. In lakes, carbonate precipitation is induced by evaporative supersaturation, with contributions from CO2 degassing and microbiological processes. Lake carbonates largely record the evaporitic enrichment (hence salinity) of the parent water which can be traced by Na, Li, B, and $\delta^{18}O$, although other factors (such as e.g., high

precipitation rates, mixing with thermal waters, groundwater, or precipitation) also affect their signatures. This study is of significance to those dealing with the fractionation of oxygen, carbon, and boron isotopes and par-titioning of elements in natural brine-carbonate environments. Furthermore, these findings contribute to the advancement in proxy development for these depositional environments.

Keywords

Lacustrine carbonate archives, brine-carbonate chemistry, partitioning coefficients, boron isotopes, Laguna del Peinado

3.1. Introduction

Carbonates form in a variety of terrestrial environments (e.g., rivers, lakes, caves, soils) and are important archives in the geological record as they reflect physical, chemical, and biological interactions (Tanner, 2010). Analysis of their isotopic and elemental signatures can provide a wealth of information about the environmental conditions and processes during their precipitation (Deocampo, 2010; Kele et al., 2011). However, the interpretation of these signatures needs to be underpinned by knowledge of the multiple factors influencing the formation and stability of carbonates as well as the incorporation mechanisms of different elements and their isotopes into their mineral structure. Initially these signals are controlled by the geochemistry and temperature of the water, the processes driving mineralisation (inorganic, biologically-controlled, -induced or -influenced), the carbonate (precursor) mineralogy, and may be complicated by disequilibrium effects during precipitation and diagenetic effects after deposition (Immenhauser et al., 2002; Leng and Marshall, 2004; Jones and Peng, 2016; Dupraz et al., 2009; Deocampo, 2010; Geske et al., 2012; Della Porta, 2015; McCormack et al., 2019; Ryves et al., 2020). Although carbonate precipitation experiments are valuable to isolate the impact of specific solution conditions on trace elements incorporation and isotopic fractionation, they are unable to simulate the complex interrelated processes of natural environments (Leng and Marshall, 2004; Mitnick, 2018, Li et al., 2020; Wassenburg et al., 2020). In light of these complexities, a more holistic approach is necessary to unravel the multifaceted controls on mineralisation and the incorporation of different elements and their isotopes in natural carbonate records. Thus, it is essential to expand studies to different active carbonate systems in a broad range of geological settings and environmental conditions to develop a more comprehensive framework for the interpretation of carbonates geochemical signatures (Kele et al., 2015; Wassenburg et al., 2020; Apolinarska et al., 2021; Mors et al., 2022).

Andean lakes have a high potential as natural laboratories to study carbonate formation processes under a wide range of conditions (e.g., Valero-Garcés et al., 1999; Beeler et al., 2020; Muller et al., 2020, 2022). The Altiplano-Puna Plateau, the second highest and largest plateau in the world (Allmendinger et

al., 1997), hosts numerous endorheic basins with permanent lakes, playa-lake, and salars where carbonate deposits and carbonate microbialites form in an active tectonic and volcanic setting (Valero-Garcés et al., 2001; Gomez et al., 2018, 2020; Bougeault et al., 2019; Muller et al., 2020; Vignale et al., 2022). These environments are governed by extreme conditions (i.e., altitude above 3000 m a.s.l., precipitation deficit, high solar radiation, large diurnal temperature variations, strong winds, and hypoxia; Garreaud et al, 2003; Morales et al., 2015), and sustain highly specialized biodiversity, ranging from large vertebrates to polyextremophilic microbial communities (Mlewski et al., 2018; Farías and Saona Acuña, 2020; Vignale et al., 2022). As a result, carbonates from this region of the Andes comprise a wide variety of types (e.g., fine-grained precipitates, travertines, microbial mats, stromatolites, oncolites, thrombolites, among others) that record a combination of local hydrological conditions, water geochemistry, and microbial activity (e.g., Laguna Pastos Grandes, Laguna Negra, Laguna Carachipampa, Laguna del Diamante, and Laguna del Peinado; Valero-Garcés et al., 1999, 2001; Gomez et al., 2014, 2018; Mlewski et al., 2018; Bougeault et al., 2019; Beeler et al., 2020; Farías et al., 2020; Gomez et al., 2020; Muller et al., 2020, 2022; Vignale et al., 2022).

In the last decade, interest in these lacustrine systems has increased as they are considered modern analogues of environmental conditions on early Earth, possible conditions for life on Mars, and the formation environments of some hydrocarbon reservoirs in continental carbonates (Morris et al., 2010; Gomez et al., 2014, 2018; Mlewski et al., 2018; Buongiorno et al., 2019; Farias and Saona Acuña, 2020; Muller et al., 2020; Vignale et al., 2022). In addition, the high sensitivity of these systems to small fluctuations in water balance (e.g., Grosjean et al., 1997; Valero-Garcés et al., 2000; McGlue et al., 2013; Santamans et al., 2021) makes their carbonate deposits promising archives for the study of past environmental and climatic changes. The carbonate record is of particular importance in the Puna Plateau, where limited instrumental records (i.e., beyond the last 30 years) and the lack of other high-resolution natural climate archives (e.g., ice cores, speleothems, tree-ring records) have hampered the understanding of regional and temporal hydro-climate dynamics (Villalba et al., 2009; Piovano et al., 2014). Previous work attempting to reconstruct hydrological changes supported by geochemical data from lacustrine carbonates has proven to be challenging due to the disagreement between different proxies because of the variety of processes potentially influencing them (e.g., high salinity intervals interpreted from Sr content that do not correlate with the $\delta^{18}O$ record; Valero-Garcés et al., 1999, 2000, 2003). Similar challenges extend to the interpretation of trace elements (Sr and Mg) in microbialites as archives of hydrological changes (e.g., Buongiorno et al., 2019). The value of the carbonate deposits of these Andean systems as modern analogues and climate archives underscores the necessity to advance our comprehension of the interrelated factors controlling their formation and geochemical signatures.

This study focuses on a high-altitude hypersaline Andean lake system located in the southern Puna Plateau (Catamarca province, Argentina). The lake, Laguna del Peinado, contains particularly abundant carbonate deposits including a variety of travertines and a large microbialite system (Valero-Garcés et al., 1999, 2001; Farías et al., 2020) and provides an ideal natural laboratory to understand the fundamental processes underpinning modern carbonate precipitation. Our study aims to unravel the processes influencing the carbonate system dynamics and promoting carbonate precipitation in the El Peinado system and the underlying factors controlling their geochemical signatures. It is intended to contribute to the advancement of proxy development within this specific depositional environments, rather than the extraction of climate data. To achieve this, we combine elemental (Ca, Mg, Na, K, B, Sr, Li, Si, Cl, SO_4) and isotopic (δ^2H_w, $\delta^{18}O_w$, $\delta^{11}B_w$) analyses of the main water sources during the observation period (2019-2021) with an investigation of the elemental (Na/Ca, Mg/Ca, Al/Ca, Sr/Ca, Li/Ca, B/Ca) and isotopic ($\delta^{18}O_{carb}$, $\delta^{13}C_{carb}$, $\delta^{11}B_{carb}$) composition of recent calcium carbonate deposits from different sub-environments across the basin. Based on these comprehensive data, we examine the elemental partition coefficients and isotopic fractionation factors, thereby shedding light on the mechanisms responsible for the carbonate formation and the distinct geochemical signatures arising in these hypersaline lacustrine environments.

3.2. Geological and environmental setting

Laguna del Peinado lake is located at 3760 m a.s.l. in the southern Puna Plateau in the Central Volcanic Zone of the Andes of Catamarca province, Argentina (26° 30' 16.87" S, 68° 5' 49.95" W; Fig. 3.1a). The lake lies in the topographically closed El Peinado basin along the Peinado lineament, a NNE-SSW fault system. Here several mafic monogenetic centers and the potentially active Peinado stratovolcano of mafic compositions (basaltic andesites and andesites, last activity dated to ~ 36 ka) are aligned (Grosse et al., 2022). To the west of the lake, the Laguna Amarga rhyolitic ignimbrites (3.7-4 Ma) crop out (Kay et al., 2010). Large volumes of magma are suggested to exist in the crust below the El Peinado area (Bianchi et al., 2013; Ward et al., 2017; Grosse et al., 2022).

Due to the topographic barrier effect of the Andes that block the moisture-bearing easterly zonal winds, this area is extremely dry with evaporation greatly exceeding precipitation (Garreaud et al., 2003, 2009; Strecker et al., 2007; Castino et al., 2017). Mean annual precipitation values are < 120 mm/yr (based on TRMM satellite data maps from 1998 to 2019, Fig. 3.1b), while evaporation has been estimated to be > 1500 mm/yr in Laguna del Negro Francisco area (27°28’ S, 69°14’ W, 4,125 m a.s.l.; Grosjean et al., 1997). The region is generally cold, with a mean annual temperature of 8°C but a large daily temperature amplitude of up to 40 °C (Valero-Garcés et al., 1999).

Laguna del Peinado is a shallow hypersaline lake (maximum water depth ~4.2 m measured during the wet season in spring 2019, this study) fed by numerous hot springs on its southern and western shores. At its southern shore, a hydrothermal pool discharges through a stream into an extensive shallow wetland area of approx. 0.7 km in length (Fig. 3.1c). At its western shore, numerous smaller marginal hot spring seeps are found. To the north of Laguna del Peinado, the smaller hypersaline lake Laguna Turquesa (estimated water depth ~1.3 m) is located and currently disconnected from the main lake due to low water level (Fig. 3.1c). Carbonates comprise a wide variety of types including microbialites (microbial mounds and mats, oncolites), travertines, and fine-grained mineral precipitates (Valero-Garcés et al., 2001; Farías et al., 2020; Della Vedova et al., 2022). Macrophytic travertines consist of an open meshwork of calcite-coated stems that occur near hydrothermal springs, along the vegetated lake margin, in the submerged littoral zone, and at the lake bottom (Valero-Garcés et al., 2001). Microbial mounds show a patchy distribution and constitute the largest known microbialite system in this region (Valero-Garcés et al., 2001; Farías et al., 2020).

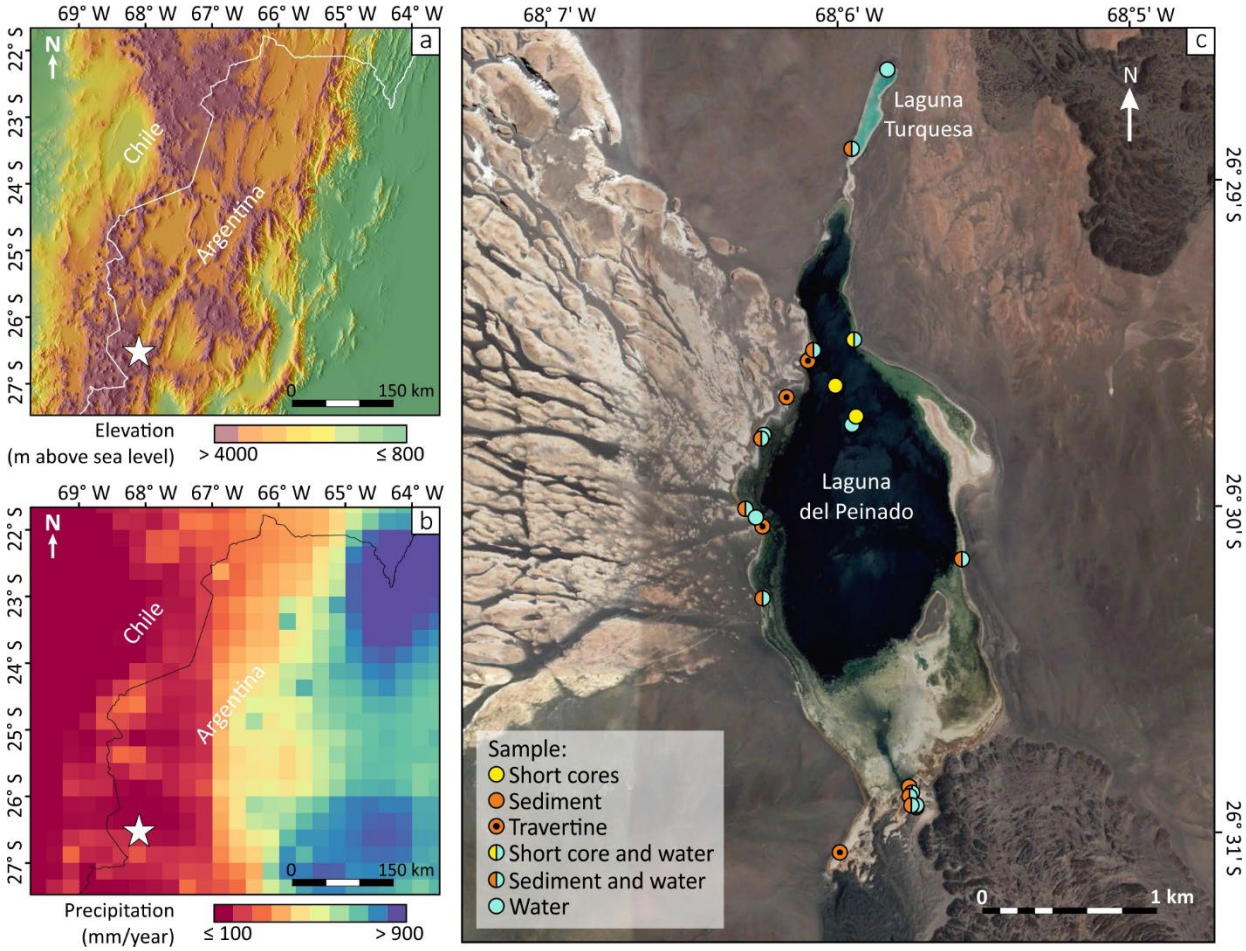

Figure 3. 1. Study area location. The white star points Laguna del Peinado location in a relief map (a) and the mean annual rainfall distribution derived from 1998 to 2019 TRMM satellite data (Huffman et al., 2007) in the Central Andes of NW Argentina (b). c) Samples location in the lake and catchment area.

3.3. Materials and Methods

3.3.1. Fieldwork and sampling

Samples for this study were collected during fieldwork in the El Peinado basin in January 2019, November 2019, and February 2021 (austral spring-summer). Water samples were collected from Laguna del Peinado (n = 7), the smaller Laguna Turquesa (n = 2), the inflowing hydrothermal springs (n = 8), and the wetlands (n = 2; Fig. 3.1c, Table S1; Vignoni et al., 2023a). Rainwater (n = 2) was sampled in the nearest town, Antofagasta de la Sierra (3320 m a.s.l.) located approx. 80 km towards the northeast, and snow (n = 2) was collected at nearly 5000 m a.s.l., 17 km southeast of the lake. Temperature, pH, electrical conductivity (EC), total dissolved solids (TDS), and salinity were measured in situ with a Hanna HI 98194 multiparameter. Water samples were vacuum-filtered with sterilized syringes and 0.22 µm/0.45 µm pore-size cellulose acetate filters (Minisart, Sartorius Stedim Biotech GmbH) and stored in polyethylene bottles at 4 °C until analyses. Samples for metal analyses were acidified with ultrapure HNO_3 (to pH < 2).

The lake bathymetry was measured using a Garmin Echosounder installed in an inflatable Zodiac boat. Short sediment cores (< 1 m) were recovered from Laguna del Peinado using a raft equipped with an Uwitec coring device. Carbonate and surface sediment samples were collected from the lakes, hot springs, and the catchment area, packed in polyethylene vials and plastic bags, and stored at 4 °C. At the GFZ Potsdam (Germany) laboratories, the cores were length-wise split into two halves, described and sampled for subsequent analyses. All samples were kept in a freezer for 24 to 48 hours and freeze-dried for 72 hours. Surface sediments were further subsampled and separated into a matrix fraction (i.e., fine material) and calcium carbonate fragments and ground to powder. A total of 33 sediment samples were analysed in this study.

3.3.2. Sample preparation and analysis

3.3.2.1. Water sample analyses

Total alkalinity (TA) was measured by open-cell titration using a 0.01 M HCl solution with a 876 Dosimat plus (Ω Metrohm) at GEOMAR (Kiel, Germany) for samples collected in 2019. For samples collected in 2021, TA was measured by end point titration using a 1.6 N H_2SO_4 solution until pH = 4.5 at CICTERRA (Córdoba, Argentina).

Major and minor ion composition in water samples was determined on an ICP-OES (Inductively Coupled Plasma-Optical Emission Spectrometry) at GEOMAR. The relative standard deviation (2RSD) based on repeated measurements of standard Atlantic seawater reference material IAPSO was 1% for Ca,

Na and Sr, 2% for Mg and Li, 3% for K, 4% for B, and 9% for Si. Anions were measured by IC (Ion Chromatography) at GFZ Potsdam with a 2RSD of 3% for Cl and 4% for SO_4.

Oxygen ($\delta^{18}O_w$) and hydrogen ($\delta^{2}H_w$) isotopic composition of water samples was measured at GFZ Potsdam with a Cavity Ring-Down Spectrometry device from PICARRO (L2130-i). Results are expressed in δ-notation in ‰ relative to VSMOW (Vienna Standard Mean Ocean Water). The analytical precision was < 0.1‰ for $\delta^{18}O_w$ and < 0.5‰ for $\delta^{2}H_w$ (SD).

Boron isotope analyses of water samples ($\delta^{11}B_w$) were performed at the University of St Andrews (UK). Prior to measurements, boron was separated from the rest of the elements in the sample using a boron-specific ion exchange resin Amberlite IRA 743. Purified boron samples were measured for their isotopic composition on a Neptune Plus (Thermo Scientific) MC-ICP-MS equipped with 10^{13} Ω resistors. Instrumental mass bias was corrected by standard-sample bracketing with a 15 ppb standard NIST SRM 951 (boric acid) that consequently converted $^{11}B/^{10}B$ ratios to δ-notations. Samples, standards and blanks were introduced to the instrument in a 0.5 M HNO_3 matrix spiked to 0.3 M HF to aid boron wash out (Zeebe and Rae, 2020). Total procedural blanks (TPBs) were used to monitor potential contamination to the sample, containing on average ~10 pg of B and hence were negligible against the typical sample size of ~ 10-20 ng B. The analytical uncertainty was assessed by repeated measurement of NIST RM 8301 (Coral) and NIST RM 8301 (Foram) processed along with samples, yielding average values of 25.05 ± 0.26 (2SD, n = 4) and 14.63 ± 0.14 (2SD, n = 1), respectively, consistent with the published values (Stewart et al., 2020).

3.3.2.2. Aqueous chemistry modelling

We used the PHREEQC software (Version 3; Parkhurst and Appelo, 2013) with the Pitzer database (pitzer.dat; Plummer et al., 1988; Appelo et al., 2014) to determine aqueous speciation of compounds, species contribution to TA, and minerals saturation indexes (SI). Input values were taken from Table S1 (Vignoni et al., 2023a). The SI is defined as:

$$SI = log \frac{IAP}{K_{sp}} \quad (1)$$

where IAP is the ionic activity product and K_{sp} is the thermodynamic solubility constant. If SI > 0, the solution is supersaturated with respect to a mineral phase and may therefore precipitate, while SI < 0 indicates that the solution is undersaturated in a considered mineral phase.

We further used PHREEQC to perform mixing and inverse models to explore the hypothetical mixing between lake-hot spring waters and the reactions necessary to achieve the composition of a given water sample. PHREEQC results are included in Tables S2 and S3 (Vignoni et al., 2023a).

3.3.2.3. Calcium carbonate samples analyses

Elemental ratios (Li/Ca, B/Ca, Na/Ca, Mg/Ca, Al/Ca, Mn/Ca, Sr/Ca, Cd/Ca, Ba/Ca, Nd/Ca and U/Ca) and boron isotope analyses of carbonate powders ($\delta^{11}B_{carb}$) were performed at the University of St Andrews. An aliquot of approx. 3-4 mg was collected into an acid pre-cleaned 1.5 ml centrifuge vial and further processed following previously established cleaning protocols (e.g., Jurikova et al., 2019, 2020) to eliminate potential oxide coatings and organic matter before dissolution in 0.5 M HNO_3. A small aliquot of (approx. 5% of total sample volume) was used for elemental determinations using a QQQ-ICP-MS (Agilent 8900). The analytical precision based on repeated analyses of in-house standards and NIST RM 8301 (Coral) measured along with samples was < 3.5% (2RSD) for all the reported ratios. This manuscript discusses the Li/Ca, B/Ca, Na/Ca, Mg/Ca, Sr/Ca, and Al/Ca results, all measured elemental data is however available in Table S4 (Vignoni et al., 2023a). The remainder of the dissolved sample was processed and analysed for $\delta^{11}B_{carb}$ using the same protocols as previously described for water samples (Section 3.2.1).

Oxygen ($\delta^{18}O_{carb}$) and carbon ($\delta^{13}C_{carb}$) isotope analysis of carbonate samples were carried out on an automated carbonate extraction device (KIEL IV) coupled to a Finnigan MAT 253 IRMS (Thermo Fisher Scientific) at the GFZ Potsdam. Results are expressed in the conventional δ-notation in ‰ relative to VPDB (Vienna Pee Dee Belemnite). Repeated measurements of the reference material NBS 19 yielded an analytical precision better than ± 0.07‰ (SD) for both $\delta^{13}C_{carb}$ and $\delta^{18}O_{carb}$.

3.3.2.4. Scanning electron microscopy and X-ray diffraction

Scanning electron microscopy (SEM) and X-ray diffraction (XRD) analyses were carried out at the GFZ Potsdam. SEM imaging was performed on a PHENOM XL Desktop SEM with BS and EDS detectors (Thermo Fischer Scientific). To determine the mineralogy, four samples were crushed and powdered to a grain size of < 62 µm for XRD measurements. XRD patterns were obtained using a PANalytical Empyrean X-ray diffractometer operating at 40 kV and 40 mA with a theta–theta goniometer, Cu-Kα radiation, automatic divergent and anti-scatter slits and a PIXcel3D detector. The diffraction data were recorded from 4.6 to 84.9° 2 Θ with a step size of 0.013° and a scan time of 58.4 s per step. The software package AXS DIFFRACplus EVA (Bruker) was used to identify minerals and select peak references from a mineralogical database.

3.3.3. Determination of partition coefficients and isotopic fractionation factors

Empirical partition coefficients for an element X ($K_{D(X)}$) were calculated using measured element/Ca ratios as follows:

$$K_{D(X)} = \frac{(X/Ca)_{carb}}{(X/Ca)_w} \quad (2)$$

where $(X/Ca)_{carb}$ is the molar ratio of a given element to Ca in calcite and $(X/Ca)_w$ is the molar ratio of the corresponding water sample. When $K_{D(X)} > 1$ the calcite is enriched in the given element with respect to the water, while $K_{D(X)} < 1$ indicate that the calcite is relatively impoverished in the element compared to water.

Boron partition coefficients ($K_{D(B)}$) were defined following Mavromatis et al. (2015) as:

$$K_{D(B)} = \frac{[B/Ca]_{carb}}{[B/CO_3^{2-}]_w} \quad (3)$$

To calculate the B/CO_3^{2-} ratio of waters, total B and CO_3^{2-} (including ion-pairs) concentrations were obtained from the PHREEQC aqueous speciation modelling (Table S2; Vignoni et al., 2023a). For practical purpose, all $K_{D(X)}$ values are presented as $K_{D(X)} \times 10^3$ in Table S5 (Vignoni et al., 2023a).

Oxygen isotope fractionation between carbonates and waters was calculated from measured $\delta^{18}O_{carb}$ and $\delta^{18}O_w$, after $\delta^{18}O_{carb}$ conversion relative to VSMOW scale following Hoefs (2015). The fractionation factor is expressed as follows:

$$\Delta^{18}O_{carb-w} = 1000 \ln \alpha_{carb-w} \quad (4)$$

, where

$$\alpha_{carb-w} = \frac{(\delta^{18}O_{carb}+1000)}{(\delta^{18}O_w+1000)} \quad (5)$$

Values $\Delta^{18}O_{carb\text{-}w} > 0$ and $\alpha_{carb\text{-}w} > 1$ indicate enrichment of the heavier isotope in carbonates relative to water.

3.3.4. Boron isotope principles and incorporation mechanisms

Boron in water is almost exclusively present as trigonal boric acid [$B(OH)_3$] and tetrahedral borate ion [$B(OH)_4^-$], with their relative proportions being pH dependent, and a constant isotopic fractionation factor between them (ε_B of 26‰; Klochko et al., 2006; Nir et al., 2015). Thus, as the relative distribution of $B(OH)_3$ and $B(OH)_4^-$ changes with pH, so does their isotopic composition. The tetrahedral borate ion $B(OH)_4^-$ is preferentially incorporated into $CaCO_3$ (Hemming and Hanson, 1992; Mavromatis et al., 2015), hence reflecting the pH conditions upon precipitation.

The pH dependence of the two B species is defined by the boric acid apparent dissociation constant pK_B^*:

$$pK_B^* = -log \frac{[B(OH)_4^-] \times a_{H^+}}{[B(OH)_3]} \quad (6)$$

where a_{H^+} is the activity of H^+. In this study, we compared two different methods for calculating pK_B^*. The first method followed Dickson (1990) who described the thermodynamics of the dissociation of boric acid in synthetic seawater over a wide range of temperatures and salinities. While this approach has been commonly used for $\delta^{11}B$-based pH reconstructions from marine archives, it does not account for variations in major ion contributions to salinity. These may be considerable in continental evaporitic settings; hence, this approach for calculating pK_B^* may not present the best choice. As the second approach, we therefore used the PHREEQC software (Parkhurst and Appelo, 2013), as previously used for example by Golan et al. (2016) and Jurikova et al. (2023) in the Dead Sea. The pK_B^* values obtained via the two different methods are summarised in Table S5 (Vignoni et al., 2023a).

Given α_B, pK_B^*, $\delta^{11}B_w$ and $\delta^{11}B_{carb}$, it is possible to calculate the pH at which $CaCO_3$ precipitated:

$$\mathrm{pH} = \mathrm{pK_B^*} - \log\left[-\frac{\delta^{11}\mathrm{B_w} - \delta^{11}\mathrm{B_{carb}}}{\delta^{11}\mathrm{B_w} - (\alpha_\mathrm{B} \times \delta^{11}\mathrm{B_{carb}}) - 10^3(\alpha_\mathrm{B} - 1)}\right] \quad (7)$$

To assess the incorporation of B species into calcite, we further calculated the $\delta^{11}B$ composition of boric acid and borate ion in the water samples ($\delta^{11}B_3$ and $\delta^{11}B_4$, respectively) following Nir et al. (2015) expressions:

$$\delta^{11}\mathrm{B_4} = \frac{\delta^{11}\mathrm{B_w} \times \mathrm{B_w} - \varepsilon_\mathrm{B} \times \mathrm{B_3}}{\mathrm{B_4} + \alpha_\mathrm{B} \times \mathrm{B_3}} \quad (8)$$

$$\delta^{11}\mathrm{B_3} = \delta^{11}\mathrm{B_4} \times \alpha_\mathrm{B} + \varepsilon_\mathrm{B} \quad (9)$$

where B_w and $\delta^{11}B_w$ are the dissolved and isotopic composition of the total boron system, B_3 and $\delta^{11}B_3$ of boric acid, B_4 and $\delta^{11}B_4$ of borate, ε_B the fractionation factor between boron species (26‰) and $\alpha_B = (10^{-3} \times \varepsilon_B + 1)$ (1.026; Nir et al., 2015). Using the measured total dissolved boron, the concentrations B_3 and B_4 (including borate-ion pairs) were obtained from the PHREEQC output (Table S2; Vignoni et al., 2023a).

3.4. Results

3.4.1. Hydro-chemistry

In the following we summarise the measured hydro-chemical characteristics of waters in the El Peinado basin as to its most recent state in 2021, for results from 2019 the reader is referred to Table S1 (Vignoni et al., 2023a) and Figure 2.

Analyses of waters from Laguna del Peinado and Laguna Turquesa indicated alkaline brines (pH = 7.8 to 8.2) with high EC, TDS, and salinity (> 60 mS/cm, > 30 g/L and > 45 psu, respectively; Table S1; Vignoni et al., 2023a). The highest values were found in Laguna Turquesa, where salinity was estimated to be 97 psu from a regression line between salinity and conductivity ($R^2 = 0.99$, Salinity (psu) =0.6806 x EC (mS/cm)

– 1.788). TA was 4.6 and 7 meq/L for Laguna del Peinado and Laguna Turquesa, respectively. Hot spring waters from the southern shore were brackish (4.6 psu), slightly acidic (pH = 6.15), with a temperature around 36 °C, and the highest TA (12.1 meq/L). Hydrothermal waters from the western shore were characterised by higher EC, TDS, and salinity values (Table S1; Vignoni et al., 2023a), more variable pH (between 5.1 and 6.5) and temperatures (between 20 and 41 °C). Waters from the wetlands showed similar, hydrothermally dominated, values for all measured parameters (Table S1; Vignoni et al., 2023a). Rain and snow waters were very dilute, with low TDS and acidic pH (Table S1; Vignoni et al., 2023a).

The major (relative abundance > 1%: Na^+, Ca^{2+}, Mg^{2+}, Li^+, B, Cl^-, SO_4^{2-}) and minor (abundance between 1% and 0.01% range: K^+, Sr^{2+}) ion composition of water samples is shown in Figure 2. The waters are sodium-chloride type. Both lakes and the western shore hydrothermal springs were Ca-rich with Mg/Ca < 1, while the hot springs at the southern shore were comparatively more enriched in Mg (with Mg/Ca ratio between 1.5 and 3.1; Fig. 3.2). Li and B concentration was high in all waters, with highest concentrations reaching values of 43.7 and 37.7 mmol/L in Laguna Turquesa, respectively (Fig. 3.2, Table S1; Vignoni et al., 2023a). Dissolved Si varied little between water samples (1.6 to 2.2 mmol/L; Table S1; Vignoni et al., 2023a). Waters in the wetland areas were more concentrated in all relevant ions when compared to the hot springs, and ion concentrations in rain and snow waters were naturally very low, yet variable between samples (Table S1; Vignoni et al., 2023a).

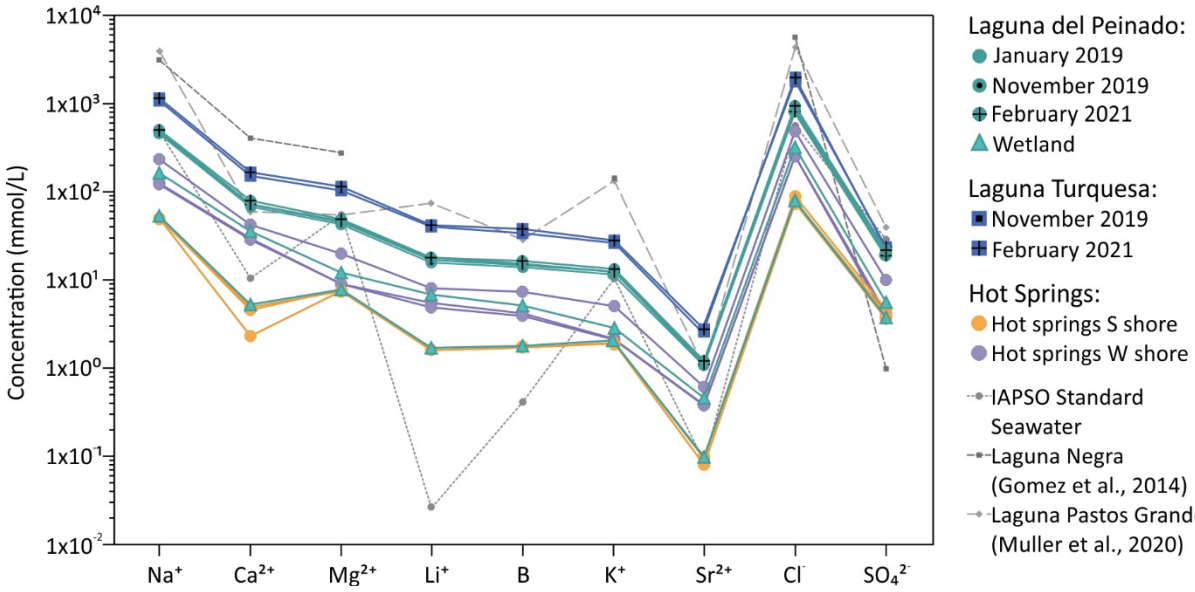

Figure 3. 2. Major and minor ion composition of waters in the El Peinado basin. Concentrations of all elements expressed in mmol/L on a logarithmic scale to allow comparison between the different water samples. Composition of mean ocean seawater (IAPSO) and brines from other lakes from the Altiplano-Puna Plateau – Laguna Negra (Catamarca, Argentina; Gomez et al., 2014) and Laguna Pastos Grandes (Southern Bolivia; Muller et al., 2020) – are also shown for comparison. For Si concentrations and the composition of rainfall and snow samples please refer to Table S1 (Vignoni et al., 2023a).

Systematic sampling during the austral spring-summer season from 2019 to 2021, showed a gradual increasing trend in EC, TDS, salinity, and dissolved ion concentrations in the lakes (Fig. 3.2, Table S1; Vignoni et al., 2023a).

3.4.2. PHREEQC modelling

Aqueous chemistry modelling using PHREEQC showed that lake brines of both Laguna del Peinado and Laguna Turquesa were supersaturated (i.e., SI > 0) with respect to calcite and aragonite (Table S2; Vignoni et al., 2023a). Positive SI for gypsum (of 0.15) was found only in Laguna Turquesa while values for Laguna del Peinado were close to equilibrium (i.e., SI ~ 0; Table S2; Vignoni et al., 2023a). Waters from the southern shore hot springs were undersaturated with respect to calcite and aragonite, except for one sample (PEI19-HTS1-3) that yielded SI > 0. Likewise, waters from the western hot springs were undersaturated, except for one sample possibly mixed with the lake water (PEI19-HTS4-1). Carbonate alkalinity (CA = $[HCO_3^-] + 2[CO_3^{2-}]$) is the main contributor to total alkalinity (TA) in all hot springs (Table S2; Vignoni et al., 2023a). In the lakes, CA represented between 37 to 74% of the TA and borate alkalinity (BA = $[B(OH)_4^-]$) between 26 and 62% (Table S2; Vignoni et al., 2023a). Modelled DIC values ranged between 39.75 and 1.71 mmol/L, with higher values in the hot springs and lower values in the lakes. Considering two samples from the western shore hot springs as outliers, DIC and CA values showed a strong covariation (r = 0.92, Fig. 3.3a).

Mixing modelling between the lake and the southern shore hot spring water showed that a mixing ratio of 10% and 90%, respectively, is necessary to reach SI = 0 with respect to calcite (Fig. 3.3b). A mixture of 15% lake and 85% hot spring water resulted in the SI for calcite observed for sample PEI21-WL-4 (Fig. 3.3b, Table S2; Vignoni et al., 2023a). For the western shore hot springs, near equilibrium conditions (calcite SI ~ 0) were reached with a mixture of 80% lake and 20% hot spring water, while a mixture with approx. 91% of lake water was needed to reach calcite SI close to that of sample PEI21-WL-3 (Fig. 3.3b, Table S2; Vignoni et al., 2023a). Mixing models for both sites showed increasing conductivity with higher percentage of lake water (Fig. 3.3c).

Inverse modelling was run to estimate the degree of mixing between the lake and the hot spring waters and the carbonate system reactions required to reach the values observed in the wetlands (within the given uncertainties; Table S3; Vignoni et al., 2023a). To constrain the number of model runs, $H_2O_{(g)}$, $CO_{2(g)}$, calcite, and gypsum were considered as reactant phases and an uncertainty of 0% was set for TA in both the initial and the final solutions. For the southern shore, the transition to the wetland sample PEI21-WL-4 involved the loss of $H_2O_{(g)}$ and $CO_{2(g)}$, and calcite precipitation from an initial solution consisting only of hot spring water (Fig. 3.3b, Table S3; Vignoni et al., 2023a). Another model showed in addition gypsum dissolution. To achieve the composition of the western shore sample PEI21-WL-3 a combination of mixing

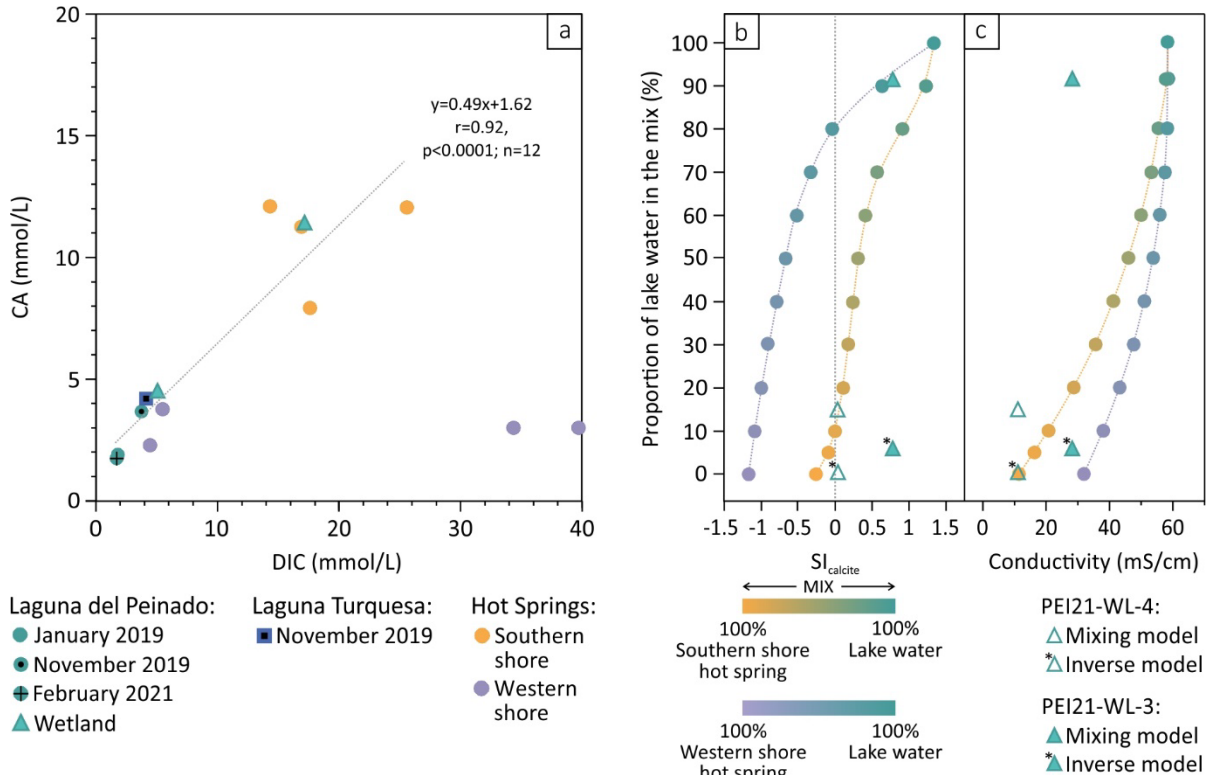

Figure 3. 3. PHREEQC geochemical modelling results. a) Carbonate alkalinity (CA) and dissolved inorganic carbon (DIC) modelled values. The two samples from western hot springs with extreme DIC values (> 30 mmol/L) were excluded from the linear regression as well as from the calculation of the Pearson's correlation coefficient (r). b) Saturation index (SI) with respect to calcite and c) conductivity values obtained considering different percentages of mixing between lake water (PEI21-WL-1) and water from the southern and western shore hot springs (PEI21-HTS1-1 and PEI21-HTS5-1, respectively). Samples from the southern and western shore wetlands (PEI21-WL-4 and PEI21-WL-3, respectively) are plotted according to the percentage of lake water required in the mixing and inverse models (marked with *) to achieve the calcite SI based on in situ observations (Table S2; Vignoni et al., 2023a). Note that the measured conductivity values for the wetland samples are lower than those resulting from the mixing model (c).

of ~94% of hot spring water with ~6% of lake water, the removal of $H_2O_{(g)}$ and $CO_{2(g)}$, and calcite dissolution was required. An alternative model also showed gypsum precipitation (Fig. 3.3b, Table S3; Vignoni et al., 2023a).

Two water samples from Laguna del Peinado shore (PEI21-WL-2 and PEI21-WL-5) and one sample from Laguna Turquesa (PEI21-LTurquesa-1) failed to converge a numerical solution based on the input parameters, suggesting that non-carbonate alkalinity in the samples might have been greater than the measured input TA value. At the measured in situ pH and B concentrations, modelled BA for each sample was 5.28, 3.42, and 12.19 meq/L, respectively (Table S6; Vignoni et al., 2023a). These values are higher than the measured TA by 0.38, 0.86, and 5.1 meq/L, respectively, meaning that aquaeous modelling required higher than measured input TA values. Because DIC was not measured and two parameters (pH, TA, DIC, pCO_2) are needed to determine the carbonate system, different scenarios were tested for comparison where pH or TA was allowed to vary (Table S6; Vignoni et al., 2023a). We also tested the

database sit.dat which resulted in a successful model for each sample. A detailed analysis of the results is beyond the scope of this work but can be found in Table S7 and Figures S1 to S4 (Vignoni et al., 2023a) where they are compared with the values obtained using the database pitzer.dat.

3.4.3. Isotopic ($\delta^{18}O_w$, $\delta^{2}H_w$, and $\delta^{11}B_w$) composition of waters

Lake brine from the Laguna del Peinado was the isotopically the heaviest with $\delta^{18}O_w$ and $\delta^{2}H_w$ values of 7.3‰ and 7.6‰, respectively, based on 2021 samples (Fig. 3.4a, Table S1; Vignoni et al., 2023a). Values for Laguna Turquesa were slightly lower, with $\delta^{18}O_w$ and $\delta^{2}H_w$ of 6.2‰ and -6.3‰, respectively. Hydrothermal springs, on the other hand, yielded considerably lighter isotopic values. Average $\delta^{18}O_w$ and $\delta^{2}H_w$ values for the southern hot spring pool were -5.9‰ and -54‰, respectively. Hot springs from the western shore showed even lower $\delta^{18}O_w$ and $\delta^{2}H_w$ values (-8.4‰ and -76.1‰, respectively). Wetland samples showed slightly higher values than those obtained from hot springs (Fig. 3.4a, Table S1; Vignoni et al., 2023a). Measured spring-summer precipitation plotted close to the Global Meteoric Water Line (GMWL; Craig, 1961) and is used to define a potential Local Meteoric Water Line (LMWL; $\delta^{2}H_w = 7.78 \times \delta^{18}O_w + 13.5$, $R^2 = 0.95$; Fig. 3.4a).

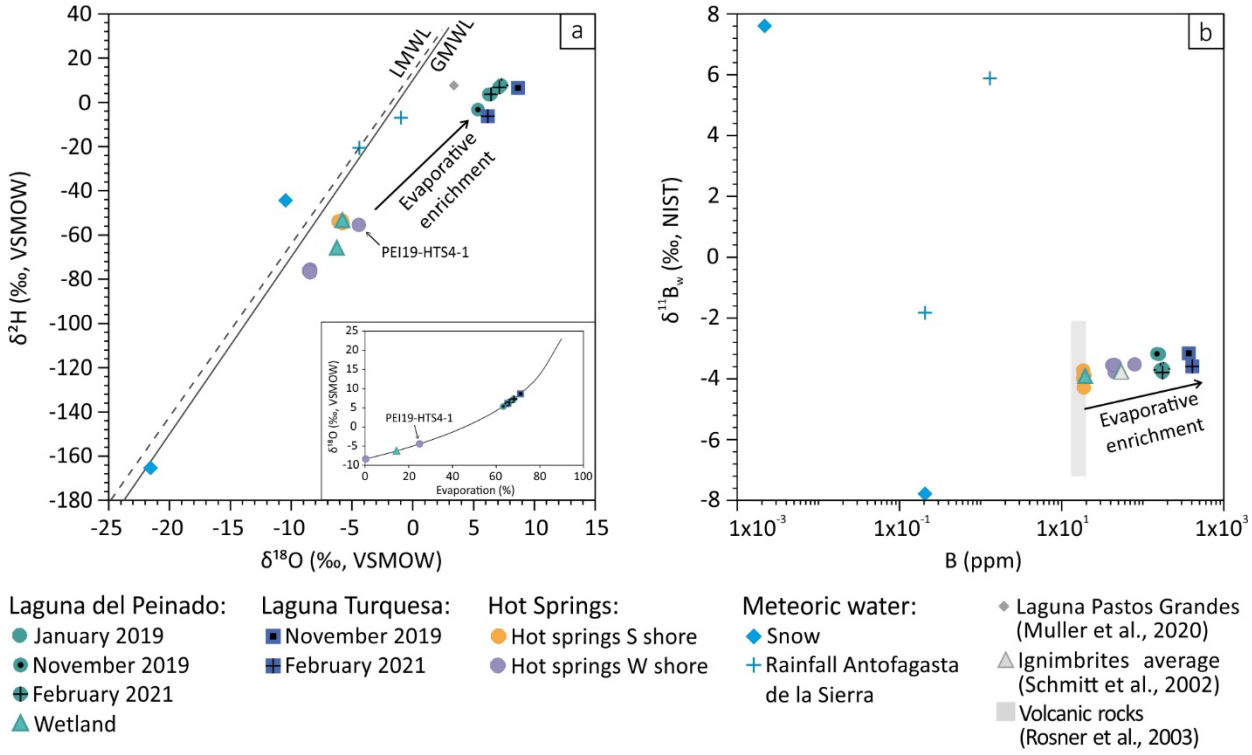

Figure 3. 4. Isotopic composition of water samples in El Peinado basin. a) $\delta^{18}O_w$ and $\delta^{2}H_w$ values. The solid line is the Global Water Meteoric Line (GWML; Craig, 1961) and the dashed line represents a potential Local Meteoric Water Line (LMWL) as defined by the precipitation samples. Right bottom corner: Rayleigh model for $\delta^{18}O_w$; the initial conditions are based on the $\delta^{18}O_w$ values of the western shore hot spring (PEI19-HTS3-1). b) $\delta^{11}B_w$ and B concentrations. Grey triangle shows the average value for ignimbrites in the Altiplano-Puna Volcanic Complex (Schmitt et al., 2002). Grey shaded bar represents the composition range of volcanic rocks from Rosner et al. (2003).

Boron isotopic composition of the hot springs and brine samples varied between -4.3‰ and -3.2‰ (Fig. 3.4b, Table S1; Vignoni et al., 2023a). Lake waters were isotopically heavier than hot springs by approx. 0.4‰ (Fig. 3.4b, Table S1; Vignoni et al., 2023a). Highest $\delta^{11}B_w$ values were found in rainwater samples from Antofagasta de la Sierra and the 2021 snow (between -1.8‰ and 7.6‰), while the lowest $\delta^{11}B_w$ value (-7.8‰) was measured in the snow sample from 2019.

3.4.4. Characterisation of carbonate samples

Macrophytic travertines were found in all areas of the basin, including nearby the hydrothermal springs, along the western and southern lake margin, in the wetlands, at the lake bottom, and approx. 10 m above the present lake level on basaltic deposits (Fig. 3.5 a, b, and c). *Cocconeis placentula* s.l. diatoms cemented with micritic calcite were commonly found in the walls of the stem-holes (Fig. 3.6a, b, and c). Some also presented microbial filament structures that consisted of mineralized fine parallel columns (Fig. 3.6d).

Carbonates in the hydrothermal springs were commonly associated with microbial mats, and were particularly abundant in the southern hot spring and stream (Fig. 3.5f and 6e). On the edges of the southern hot spring pool, microbialites consisted of alternating layers of red-pink microbial mats of a few milimeters thick and calcium carbonate layers up to ~1 cm thick (Fig. 3.5f). At the bottom of the pool and stream, carbonate precipitates were found underneath green mats consisting of fine-grained calcite and diatoms, sometimes in aggregates.

Surface sediments collected from short cores (Fig. 3.1c, Table S4; Vignoni et al., 2023a) comprised macrophytic travertines, aquatic macrophytes (*Myriophyllum* or *Potamogeton*), and matrix (Fig. 3.6c and f). The travertines consisted of thin beige and/or grey stalks in an open meshwork arrangement, filled with a matrix composed of fine-grained calcite, halite, diatoms, and organic matter remains (Fig. 3.6f). SEM imaging of travertines revealed abundant infill with *Cocconeis placentula* s.l. diatoms and mineralized microbial structures (Fig. 3.6c). Sediments collected from the shore of the lake and wetlands were formed mainly by diatom-carbonate aggregates, travertines clasts, halite (Fig. 3.6g and h), and variable amounts of medium to coarse volcanic sand, particularly common in samples from the northwestern shore. The single available sample from the shore of Laguna Turquesa consisted of a thin calcite crust with diatoms and halite present (Fig. 3.6i).

XRD analyses revealed calcite as the main $CaCO_3$ polymorph in all but one sample from the southern hot spring, which contained both calcite and aragonite (Fig. 3.6j). SEM images confirmed the presence of calcite in all samples, with no observations of aragonite (Fig. 3.6a to i).

The different carbonate samples are shown in tables and figures according to the location or sub-environment from which they were collected (Table S4; Vignoni et al., 2023a).

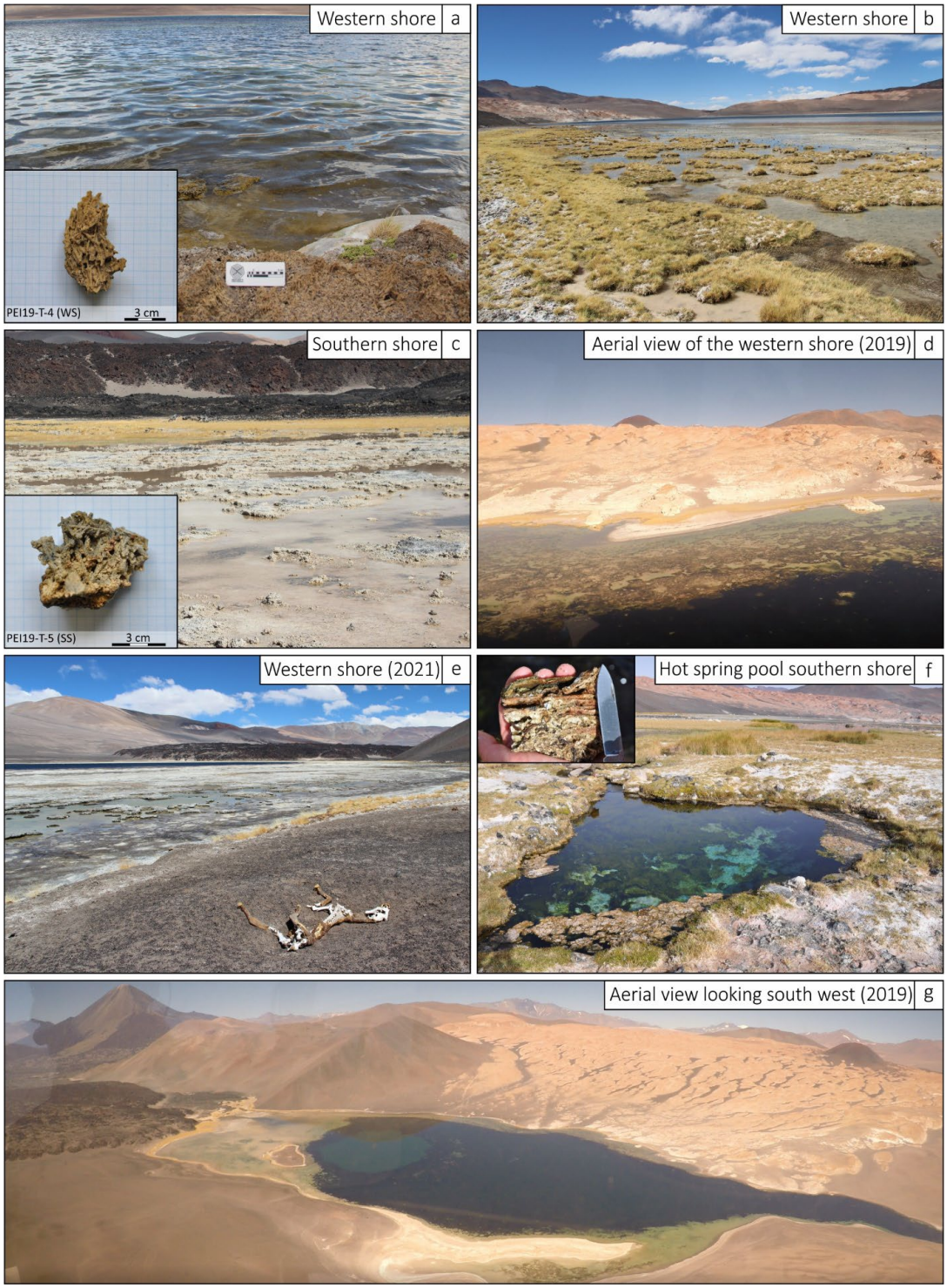

Figure 3. 5. Macrophytic travertines a) above the lake level, b) coating macrophyte stems on the western shore and c) emerging in the wetland area in the southern shore. d) Aerial view of the western shore microbialites system in 2019. e) Western shore microbialites in 2021. f) Hot spring pool on the southern shore. g) Aerial view of Laguna del Peinado in 2019.

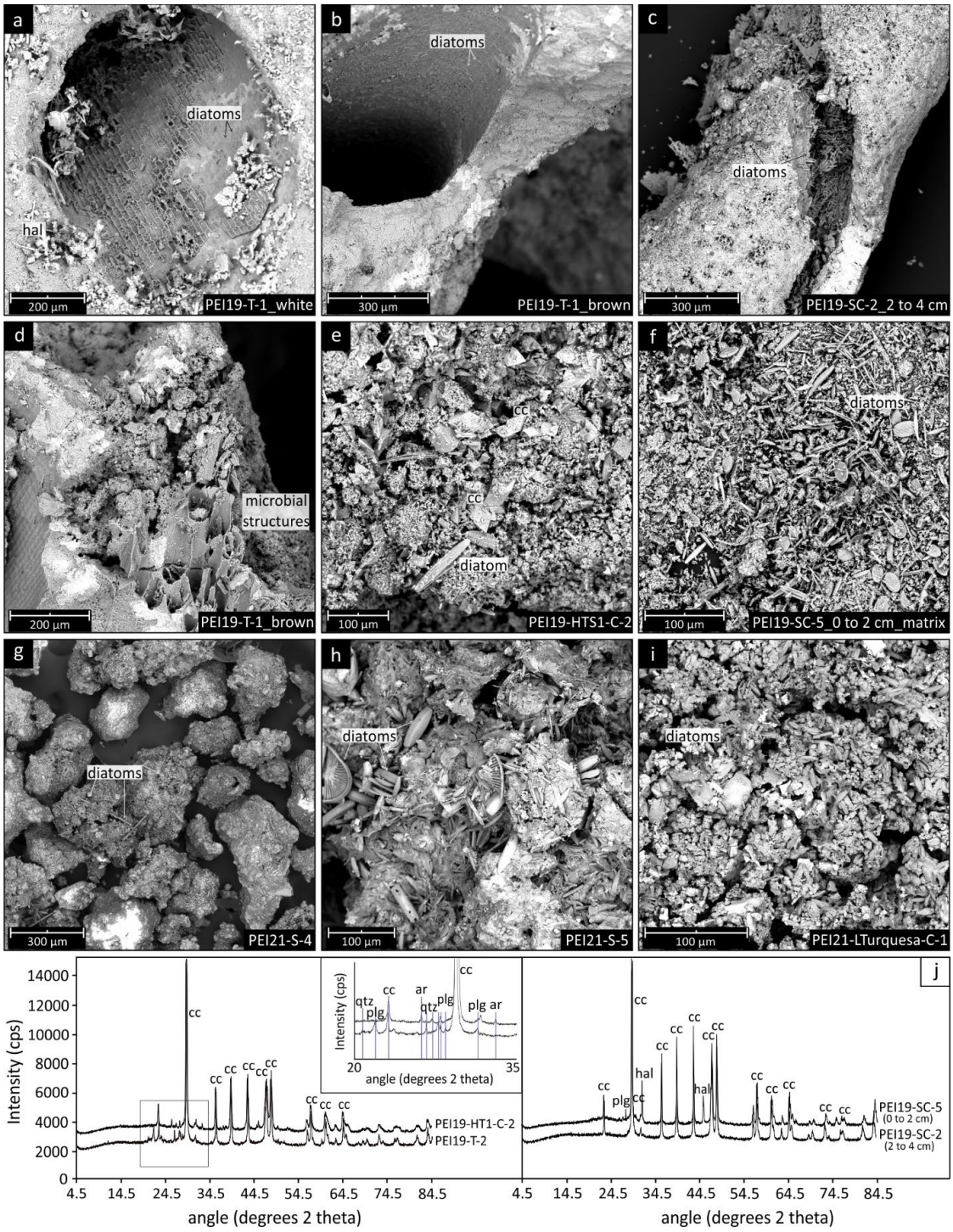

Figure 3. 6. a to i) Scanning electron microscope (SEM) images of travertine and sediment samples from the El Peinado basin. j) XRD diagrams of the analysed samples. cc = calcite, ar = aragonite, hal=halite, plg= plagioclase, qtz=quartz.

3.4.5. Elemental and isotopic composition of carbonates

Chemical composition varied strongly between samples (Fig. 3.7, Table S4; Vignoni et al., 2023a). Mg/Ca ranged between 15 and 69 mmol/mol, with lower values found in the lake samples and higher values in the southern samples. Calcites from the western shore and lakes showed a narrow range in Sr/Ca (mean 5 mmol/mol), while those collected from the south showed a larger variability (between 2.3 and 11 mmol mol^{-1}). Lake and western calcites had generally higher Na/Ca, Li/Ca, and B/Ca content compared to the southern ones, reaching up to 14 mmol/mol for Na/Ca, 2006 µmol/mol for Li/Ca and 4383 µmol/mol for B/Ca. Calcite from Laguna Turquesa recorded the highest Li/Ca and B/Ca values (Fig. 3.7, Table S4; Vignoni et al., 2023a).

The $\delta^{18}O_{carb}$ values varied between -4.6‰ and 6.7‰, and $\delta^{13}C_{carb}$ varied between 4.3‰ to 9.4‰ (Fig. 3.8a, Table S4; Vignoni et al., 2023a). Lowest values (for both $\delta^{18}O_{carb}$ and $\delta^{13}C_{carb}$) were measured in samples associated with the southern hot springs, while western samples were comparatively isotopically heavier. Lake calcites exhibited the highest $\delta^{18}O_{carb}$ (between 5.4‰ and 6.2‰), with $\delta^{13}C_{carb}$ between 7.2‰ and 9.2‰ (Fig. 3.8a, Table S4; Vignoni et al., 2023a).

The $\delta^{11}B_{carb}$ values varied between -22.8‰ and -32.6‰ (Fig. 3.8b, Table S4; Vignoni et al., 2023a). The lowest $\delta^{11}B_{carb}$ values corresponded to surface lake sediments from one of the short cores (PEI19-SC-5). Samples from the southern shore had relatively higher $\delta^{11}B_{carb}$, while calcites from the western shore covered a wider range of values (between -24.6‰ and -30.8‰).

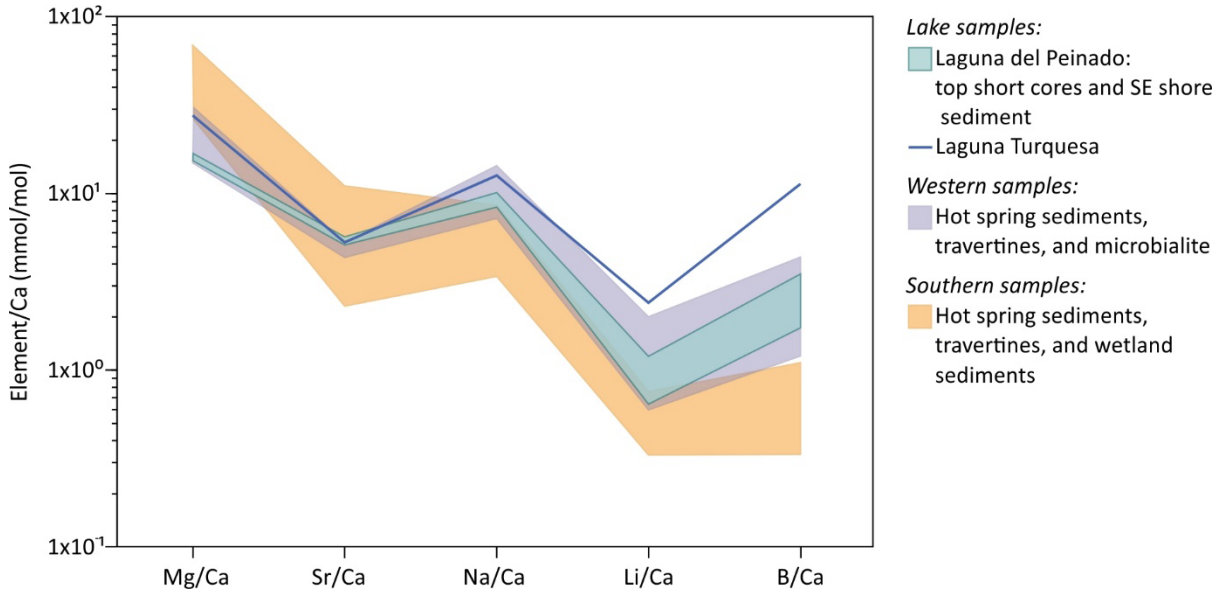

Figure 3. 7. Carbonate elemental composition. Concentrations are shown as ratios with respect to calcium and are displayed in mmol/mol (element/Ca) for comparison purposes.

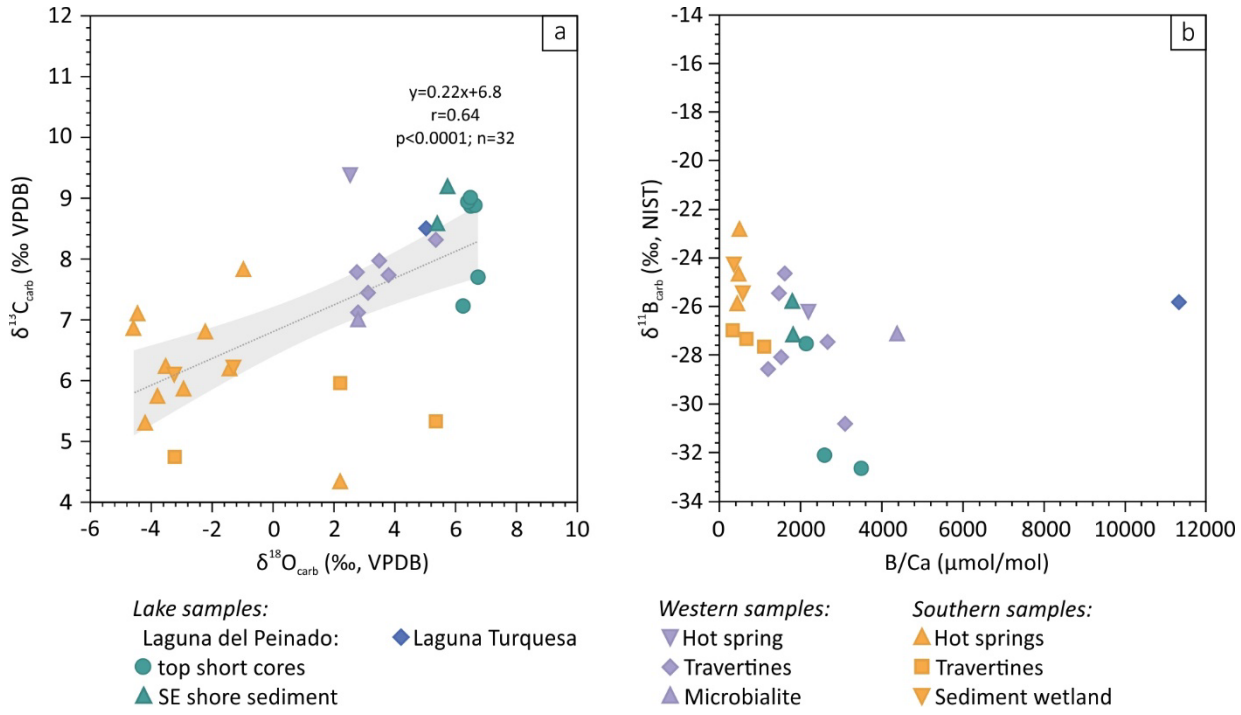

Figure 3. 8. Carbonate a) $\delta^{18}O_{carb}$ and $\delta^{13}C_{carb}$ composition. The grey area represents the 95% confidence interval. b) $\delta^{11}B_{carb}$ and B/Ca values. The x-axis is presented in logarithmic scale for better visualisation of the data.

3.4.6. Partition coefficients and fractionation factors

Partition coefficients for Mg, Sr, Na, Li, and B ranged between 8-91, 66-578, 0.2-2.4, 0.5-9.5, and 0.0001-0.02 (x 10^3), respectively (Fig. 3.9 and 10, Table S5; Vignoni et al., 2023a). In general, southern samples had the lowest $K_{D(Mg)}$, $K_{D(Na)}$, and $K_{D(Li)}$. Conversely, the highest $K_{D(Mg)}$, $K_{D(Na)}$, and $K_{D(Li)}$ values corresponded to samples from the western shore, with lake samples falling in between (Fig. 3.9, Table S5; Vignoni et al., 2023a). Both lowest and highest $K_{D(Sr)}$ were recorded in the south, contrasting with less variable values from the lake and the western side (Fig. 3.9). Highest $K_{D(B)}$ values corresponded to samples from Laguna del Peinado and a microbialite from the western shore, while samples from the southern shore and the western hot springs showed values below 0.003 (x 10^3; Fig. 3.10). Linear regression of $K_{D(B)}$ values showed a strong significant positive correlation with total dissolved B and $B(OH)_4^-$ concentration (Fig. 3.10a and b). $K_{D(B)}$ values for the Laguna Turquesa sample, Laguna del Peinado southeast sediments, and a western shore travertine could not be calculated as the CO_3^{2-} concentration of the corresponding water sample could not be modelled at the measured pH (Eq. 3). When considering all B/Ca values, a significant strong positive correlation with total dissolved B and a low correlation with measured pH was observed (Fig. 3.10c and d).

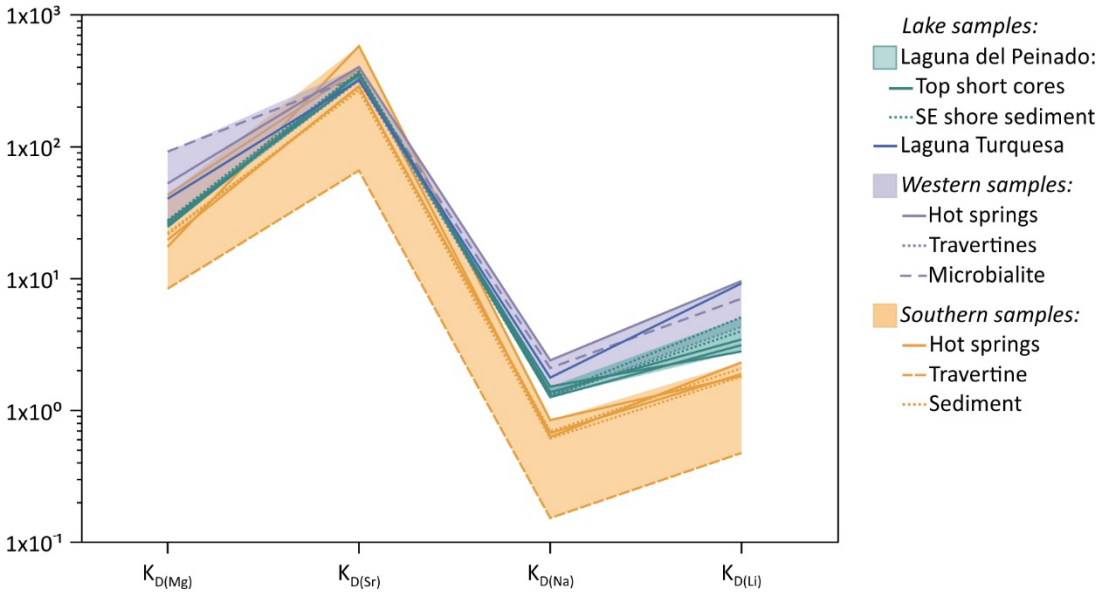

Figure 3. 9. Partition coefficients $K_{D(X)}$ of Mg, Sr, Li, and Na between water and carbonates. $K_{D(X)}$ values are reported as $K_{D(X)} \times 10^3$ for practical purposes.

Obtained $\Delta^{18}O_{carb\text{-}w}$ values ranged between 29‰ and 41‰ (Table S5; Vignoni et al., 2023a) and are shown plotted against water temperature (Fig. 3.11). Lowest $\Delta^{18}O_{carb\text{-}w}$ corresponded to lake samples, while samples from the southern and western waters showed the highest $\Delta^{18}O_{carb\text{-}w}$.

Measured $\delta^{11}B_{carb}$ were compared to the $\delta^{11}B$ composition of aqueous borate ion at in situ conditions ($\delta^{11}B_4$; Fig. 3.12). When plotted against the predicted $\delta^{11}B_4$, samples from the southern shore were offset above the 1:1 relationship ($\delta^{11}B_{carb} = \delta^{11}B_4$), with lake and western samples scattered above and below the 1:1 line.

3.5. Interpretation and discussion

3.5.1. Origin and evaporitic evolution of waters in the El Peinado basin

The potential LMWL constructed from the isotopic composition of precipitation in the vicinity of the study area is in general agreement with the LMWL proposed for northern Chile (Boschetti et al., 2019), the Altiplano-Yungas of Bolivia (Gonfiantini et al., 2001), and the northern Puna Plateau (Rohrmann et al., 2014; Peralta Arnold et al., 2017). The brackish hot springs are the principal water contributors to the hypersaline Laguna del Peinado. Their $\delta^{18}O_w$ and $\delta^{2}H_w$ values plot close to the GMWL-LMWL, supporting a meteoric provenance of water in the hydrothermal reservoir (Fig. 3.4a, Table S1; Vignoni et al., 2023a) as in other Andean hydrological and hydrothermal systems (e.g., Peralta Arnold et al., 2017). Due to the hyper-arid conditions at present, most of these lacustrine systems are sustained by old groundwater that likely formed during wet periods in the past (Latorre et al., 2006; Placzek et al., 2009; Gayo et al., 2012),

with relative contribution of modern water (< 60 years old) being minimal and spatially scarse, or almost non-existent as evidenced by the zero ^{3}H activity observed in lake waters of the Carachi Pampa basin (~ 50 km east of the El Peinado basin; Moran et al., 2019; Boutt et al., 2021; Frau et al., 2021). The observed positive shift with respect to the GMWL-LMWL likely results from evaporative enrichment (i.e., prior to infiltration, during fluids ascent; Muller et al., 2020 and references therein), moisture recycling (Godfrey

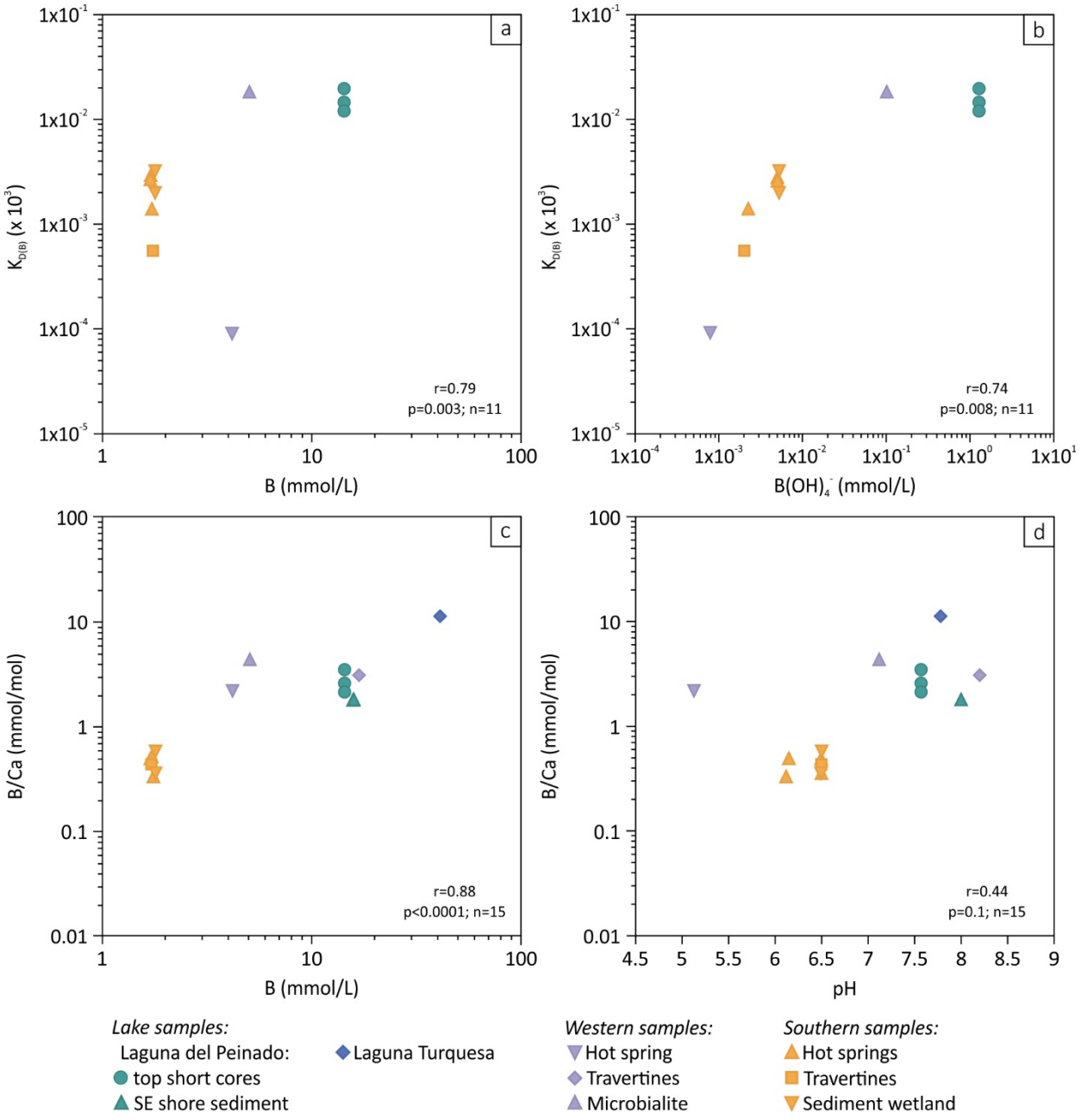

Figure 3. 10. Boron partition coefficients ($K_{D(B)}$) relative to water a) total B and b) $B(OH_4)^-$ concentrations. Carbonate B/Ca (mmol/mol) relative to water c) total B and d) pH. $K_{D(B)}$ values are reported as $K_{D(X)}$ x 10^3 for practical purposes. The axes are plotted in logarithmic scale for a better visualisation of the data. Pearson's correlation coefficients (r) describe the linear correlation between the different variables. These coefficients were calculated from the original data, without logarithmic transformation.

et al., 2003), water-rock interaction, and/or some contribution of magmatic water (Peralta Arnold et al., 2017).

The physicochemical characteristics (high TDS, high DIC, acidic, and warm) and elevated concentrations of dissolved Li and B (Table S1 and S2; Vignoni et al., 2023a) are typical of hydrothermal fluids associated with volcanic activity (Giggenbach, 1988; Chiodi et al., 2019; Mors et al., 2022). CO_2 and other gases in the hydrothermal reservoir likely derive from magma degassing, which is consistent with the young volcanism in the El Peinado basin (Grosse et al. 2020, 2022), the presence of magma reservoirs (Bianchi et al., 2013; Ward et al., 2017), and the large reservoir effect in ^{14}C ages of modern aquatic plants from the hot springs (up to > 26 000 ^{14}C years; Vignoni et al., 2023b). The low $\delta^{11}B_w$ values are interpreted to derive from the

interaction of waters with local volcanic host rocks as they are within the range of those reported for hot springs and salt-lake waters in the western Puna Plateau (-4.1‰ to +5.7‰; Schmitt et al., 2002; Kasemann et al., 2004) and are consistent with inherited B from the volcanic bedrock (Fig. 3.4b; Schmitt et al., 2002; Rosner et al., 2003).

Water supplied by hydrothermal springs to the lake is modified through evaporation, which is evidenced by the increasing EC, TDS, salinity, and dissolved ions concentrations (Fig. 3.2, Table S1; Vignoni et al., 2023a). Laguna del Peinado waters show concentration of dissolved elements approx. 9 times higher than the southern shore hot springs and 2.5 times higher compared to the ones on the western shore (Fig. 3.2). Laguna Turquesa, which became isolated from Laguna del Peinado around 2005 (Villafañe

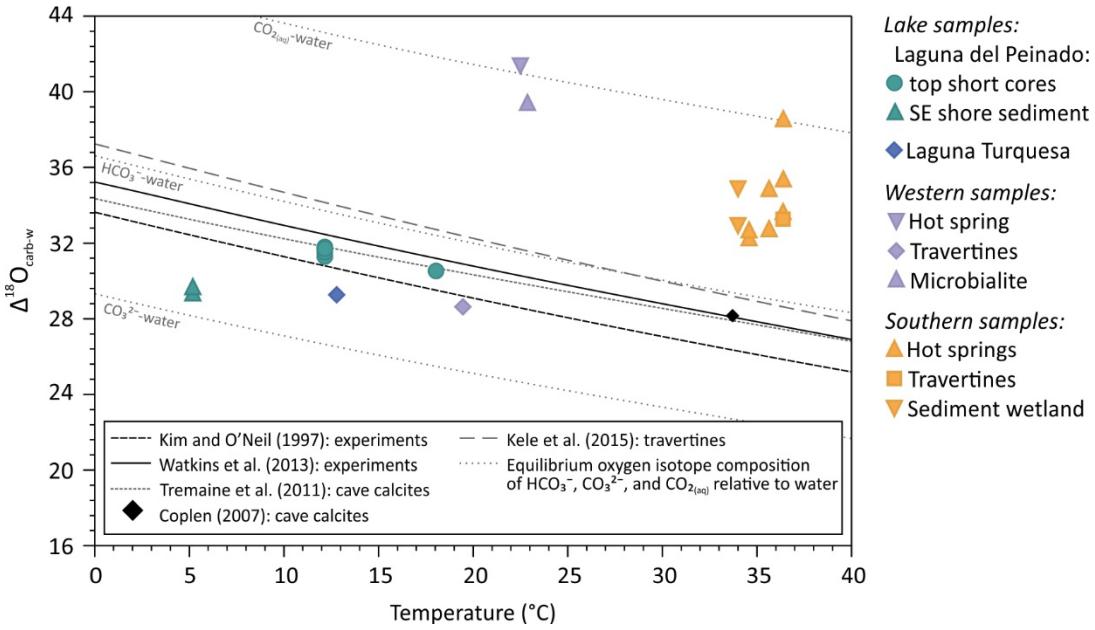

Figure 3. 11. Fractionation factor $\Delta^{18}O_{carb\text{-}water}$ between carbonates-lake/hot spring water and temperature for the El Peinado basin. The equilibrium curves proposed by Kim and O'Neil (1997), Watkins et al. (2013), Tremaine et al. (2011), Coplen (2007), and Kele et al. (2011) are included. The equilibrium oxygen isotope composition of the DIC was calculated following Zeebe (2007).

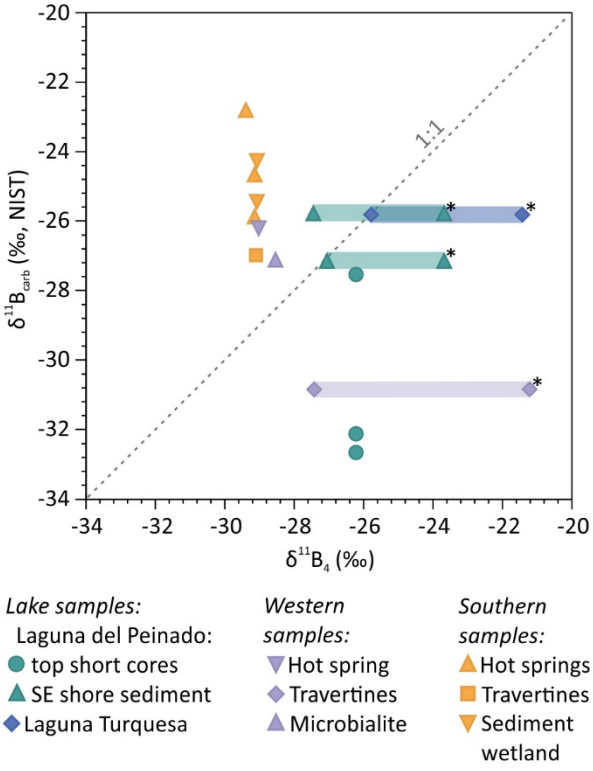

Figure 3. 12. Measured $\delta^{11}B_{carb}$ and calculated water $\delta^{11}B_4$ composition (at the measured pH) following Nir et al. (2015). The dashed line represents the 1:1 relationship ($\delta^{11}B_{carb} = \delta^{11}B_4$). For samples that failed to converge to a numerical solution, a range of plausible $\delta^{11}B_4$ values was calculated based on in situ measured pH (marked with *) and $\delta^{11}B_{carb}$-derived pH.

et al., 2021), shows the highest concentration of dissolved elements (Fig. 3.2) and thus represents the evaporitic end-member of the system. The evaporitic trend is also interpreted from the strong enrichment in heavy isotopes relative to the inflowing waters (Fig. 3.4). Considering a Rayleigh type fractionation, more than 60% of evaporation accounts for the observed ^{18}O and ^{2}H enrichment (Fig. 3.4a). The progressive increasing $\delta^{11}B_w$ values support ongoing evaporitic evolution, driven by the co-precipitation of $^{10}B(OH)_4^-$ in carbonate and gypsum evaporitic minerals (Jurikova et al., 2023). The strong evaporative trend has intensified in the El Peinado basin and regionally since the mid-1980s due to increasing air temperature and decreasing precipitation (Frau et al., 2021; Santamans et al., 2021) and was evident during the study period (2019 to 2021) with decreasing lake levels, increasing salinity, EC, TDS, and dissolved element concentrations observed between the years (Fig. 3.2, Table S1; Vignoni et al., 2023a).

3.5.2. Carbonate precipitation pathways

In the El Peinado basin, as in other hypersaline and hydrothermal environments in general, a variety of physicochemical and biological processes operating at different scales affect the carbonate system and favour carbonate precipitation: CO_2 degassing, evaporation, water mixing, and microbial activity (Gomez et al., 2014, 2018; Beeler et al., 2020; Mors et al., 2022; Muller et al., 2022).

Magma derived CO_2 fluxes into the hydrothermal reservoir explain the observed acidic pH, high DIC, and undersaturation with respect to calcite (i.e., SI < 0) in the hot spring waters, whereas towards the lake we observe a decrease in DIC and CA, higher pH, and calcite supersaturation (i.e., SI > 0, Fig. 3.3a, Table S1 and S2; Vignoni et al., 2023a). We estimated the CO_2 partial pressure (pCO_2) in the hot spring waters to be between 6 and 164 kPa (Table S2; Vignoni et al., 2023a), which is well above the atmospheric pCO_2 estimated for the Puna region at ~ 4000 m a.s.l. of 0.23 kPa (Mors et al., 2022). This suggests strong CO_2 degassing in the hot spring waters due to the pronounced pCO_2 gradient with the atmosphere, which declines towards the lake as pCO_2 drops (Table S2; Vignoni et al., 2023a). The progressive loss of CO_2

decreases DIC without changing CA and increases the pH, favouring carbonate precipitation (Zeebe and Wolf-Gladrow, 2001). High evaporation rates increase DIC and Ca^{2+} concentration explaining the brine supersaturation with respect to calcite (i.e., SI > 0, Table S2; Vignoni et al., 2023a). Calcite precipitation, in turn, causes a decrease in DIC and CA in a 1:2 ratio and lowers the pH as the carbonate equilibrium shifts to higher CO_2 levels (Zeebe and Wolf-Gladrow, 2001). The net balance of these processes explains the increase in pH and decrease in DIC and CA in a ~2:1 ratio as the hydrothermal waters evolve into the lake, and indicates a higher rate of DIC removal compared to CA (Fig. 3.3a). On a large scale, CO_2 degassing, evaporation, and calcite precipitation are thus the main processes driving changes in DIC and CA in these systems, which is also supported by the inverse modelling results (Table S3; Vignoni et al., 2023a). Moreover, the loss of CA by carbonate precipitation in high ionic strength environments also explains B becoming the major buffer contributing to TA in both the Laguna del Peinado and the Laguna Turquesa, where BA accounts for ~ 26 to 60% of the TA of the brines (Table S2; Vignoni et al., 2023a). Similar observations have been also made in the Dead Sea, where BA comprise ~ 60% of the TA (Golan et al., 2016).

Mixing between hot springs and hypersaline lake water, in addition to CO_2 degassing and evaporation, is interpreted to play a role in the increase of calcite SI on the western margin of the El Peinado system as shown by geochemical modelling (Fig. 3.3a and b; Table S3; Vignoni et al., 2023a). In fact, the occurrence of the microbial mounds system in this region (Valero-Garcés et al., 2001; Farías et al., 2020) suggests that the combination of these processes is key for its development. Microbialites within water mixing zones have also been described in other Andean lakes (e.g., Gomez et al., 2014; Buongiorno et al., 2019) underscoring the relevance of this process in sustaining these ecosystems.

On a microenvironment scale, the observed close association of carbonates with microbial communities in the El Peinado basin (e.g., calcite-diatom aggregates, mineralised microbial structures, cemented epiphytic diatoms *Cocconeis placentula* s.l., microbial mats, microbial mounds; Fig. 3.4 and 5) indicates their fundamental role in the formation of microbialites (Dupraz et al., 2009). Recent studies reported the predominance of Bacillariophyta, Crytophyta, and Cyanobacteria in the phytoplankton of Laguna del Peinado (Frau et al., 2021). Microbial communities control chemical gradients, supply crystal nucleation sites, and trap and bind suspended particles (Gomez et al., 2018; Mors et al., 2022; Shiraishi et al., 2022 and references therein). Diatoms and bacteria also produce exopolymeric substances (EPS) that act as nucleation sites allowing primary grains to bind and grow into larger calcite crystals (Gomez et al., 2018; Mlewski et al., 2018 and references therein). Photosynthetic activity additionally consumes CO_2 resulting in a local pH increase that favours carbonate precipitation. Contrary to previous assumptions that under high DIC conditions photosynthesis may not induce carbonate precipitation (Arp et al., 2001),

recent studies in hydrothermal systems in Japan have shown that photosynthetically-induced carbonate precipitation may indeed occur in high DIC environments, albeit to a lesser extent (Shiraishi et al., 2022). This could be explained by a local reduction in DIC (by degassing and evaporation) within microbial mats to a degree that photosynthetic activity can increase saturation sufficiently for calcite precipitation (Muller et al., 2022). Such mechanism likely explains the occurrence of calcite in El Peinado hot springs, and highlights well the important role both large-scale basin-wide and microenvironment processes play on carbonate precipitation.

3.5.3. Controls on calcite geochemistry during precipitation from brines and hydrothermal fluids

The observed large variations in the geochemical composition of the different carbonates are controlled by the water chemistry of the specific sub-environment in which they formed (i.e., lakes, hot springs, wetlands) and the dominant processes driving precipitation. To explore and interpret these variations, we use the partition coefficients and fractionation factors between the carbonates and the waters from which they precipitated. It is to be noted that the water composition used for deriving our $K_{D(X)}$ and fractionation factors corresponds to the conditions at the time of sampling, while the carbonates may integrate variations over longer time spans (e.g., diurnal, seasonal), in particular, travertines and microbialites that form over longer timescales (Muller et al., 2022). However, despite the increase in dissolved ion concentrations in both lakes from 2019 and 2021, the difference in water element/Ca ratios between one year and the other does not impact the observed trends in $K_{D(X)}$ values. Likewise, it is unlikely that any variations in the isotopic composition of the water affected the calculated fractionation factors, as these are homogenised by water volume and reflect rather longer-term conditions (Li et al., 2020). We thus consider our water samples to be reasonably representative of the solution composition over the span of the modern carbonate precipitation and valid for deriving the $K_{D(X)}$ values and fractionation factors.

In the following sections, we explore the incorporation of elements and fractionation of isotopes during calcite precipitation in the hot springs and hypersaline lacustrine environments. Our overall $K_{D(X)}$ values are higher than values obtained from inorganic precipitation experiments, which is in line with observations from an active travertine system in California (Mitnick, 2018) and has been attributed to the more complex environmental conditions in natural systems that are difficult to simulate in laboratory experiments (e.g., Morse and Bender, 1990; Rimstidt et al., 1998; Mitnick, 2018).

3.5.3.1. Controls on the elemental composition

The incorporation of Mg^{2+} into calcites was found to be influenced by the solution Mg/Ca, with higher $K_{D(Mg)}$ occurring at lower Mg/Ca and vice versa, as suggested from precipitation experiments (Mucci and Morse, 1983; Morse and Bender, 1990; Mitnick, 2018). This is evidenced by the overall highest Mg/Ca in southern shore calcites (Fig. 3.7, Table S4; Vignoni et al., 2023a) precipitating from hydrothermal waters characterised by Mg > Ca trend (Fig. 3.2, Table S1; Vignoni et al., 2023a) and thus lower $K_{D(Mg)}$ values (Fig. 3.9, Table S5; Vignoni et al., 2023a). In contrast, lower Mg/Ca ratios were observed in calcite where Ca > Mg waters prevail, such as both lakes and the western shore sub-environments, resulting in higher $K_{D(Mg)}$ values (Fig. 3.9, Table S5; Vignoni et al., 2023a). We did not observe Mg/Ca variations as a function of temperature (e.g., Katz, 1973; Gascoyne, 1983; Day and Henderson, 2013), which is expected considering the large variability in the water Mg/Ca which would obscure any potential temperature signal.

Our calculated $K_{D(Sr)}$ values did not show any significant correlation with other $K_{D(X)}$ or the water geochemistry except for Sr/Ca content (Table S8; Vignoni et al., 2023a). Possibly, as crystal growth experiments have shown, Sr^{2+} incorporation is influenced by the $MgCO_3$ content of calcite as Mg^{2+} incorporation produces a deformation in the crystal lattice allowing to accommodate larger cations like Sr^{2+} (Mucci and Morse, 1983) and/or calcite growth rates (Gabitov et al., 2014 and references therein).

The gradual increase in Na^+ and Li^+ in calcites from sediments, travertines, and microbialites from the less saline southern hot springs towards the more concentrated lake brines of Laguna del Peinado and the evaporitic end-member Laguna Turquesa (Fig. 3.7) suggests salinity is the primary control, as also evidenced by the significant positive correlations with $K_{D(Na)}$ and $K_{D(Li)}$ (Table S8; Vignoni et al., 2023a). This is in agreement with laboratory experiments showing interstitial incorporation of Li^+ and Na^+, and hence K_D increase at higher solution concentrations (i.e., salinity; Ishikawa and Ichikuni, 1984; Marriott et al., 2004). However, the hot spring and microbialite calcite samples from the western shore, with comparatively less saline waters due to the inflow of spring water into this sub-environment, presented higher $K_{D(Na)}$ and $K_{D(Li)}$ than the brine samples (Fig. 3.9). Likewise, travertines also showed elevated Na^+ and Li^+ content (Fig. 3.7). This is probably related to higher precipitation rates promoted by CO_2 degassing and microbial activity causing defects in the crystal lattice that allow higher Na^+ and Li^+ entrapment as observed in precipitation experiments (Füger et al., 2019).

Boron incorporation was found to increase at higher total dissolved B and $B(OH)_4^-$ concentrations, with the highest B/Ca recorded in the calcite sample from Laguna Turquesa (Fig. 3.7 and 10, Tables S4 and S5). Higher B uptake with increasing concentration of B and sodium chloride of the parent fluid has been reported for synthetic calcite (Kitano et al., 1978; Hemming et al., 1995). More recently, Henehan et al. (2022) observed a close correlation between Na^+ and B enrichment in calcite and proposed a paired

incorporation of Na^+ and $B(OH)_4^-$ in place of Ca^{2+} and CO_3^{2-} to maintain the charge balance. This would explain the mechanism by which salinity, or water Na^+ concentration, favours the incorporation of B into the crystal lattice (Henehan et al., 2022). According to our results, B enrichment correlates with higher water salinity as well as $K_{D(Na)}$ and $K_{D(Li)}$ values (Table S8; Vignoni et al., 2023a). As $B(OH)_4^-$ concentration depends on pH and total B (salinity), increased $K_{D(B)}$ could also be explained by higher pH (Fig. 3.10a and b) as expected from boron speciation principles and found during experimental precipitation of calcite (Mavromatis et al., 2015).

3.5.3.2. Controls on the $\delta^{18}O_{carb}$ and $\delta^{13}C_{carb}$ signatures

The $\delta^{18}O_{carb}$ at equilibrium is controlled by the isotopic composition of the water, the temperature at precipitation, and the relative proportion of the DIC species (Hoefs, 2015). In the El Peinado basin, $\delta^{18}O_{carb}$ values vary broadly from -4.6‰ to 6.7‰ between the different locations (Fig. 3.8a) suggesting different controlling factors involved. We observed positive $\delta^{18}O_{carb}$ values (average 6.1‰) in calcites from the short cores, the southeastern shore of Laguna del Peinado, and the crust from Laguna Turquesa. This is in line with the ^{18}O-enrichment observed in the brines due to the evaporative effect and longer residence time (Fig. 3.4a and 8a). This suggests that the $\delta^{18}O_{carb}$ signal of these calcites largely record the parent water isotope signal. If calcite precipitated under thermodynamic isotopic equilibrium conditions and water temperature was controlling the oxygen isotopes fractionation, the $\Delta^{18}O_{carb\text{-}w}$ values for these samples should plot around the oxygen isotope equilibrium lines at the measured water temperatures (Fig. 3.11). Only the three bulk calcite samples from the short cores revealed $\Delta^{18}O_{carb\text{-}w}$ values between the isotopic equilibrium curves defined by Kim and O'Neil (1997) and Watkins et al. (2013), and are in good agreement with the curve for cave calcites defined by Tremaine et al. (2011) (Fig. 3.11). This suggests that only calcite in the lake at the core locations precipitated under apparent thermodynamic isotopic equilibrium conditions.

In contrast, bulk samples from the southeastern shore of Laguna Peinado and the calcite crust from Laguna Turquesa shore were offset towards lower $\Delta^{18}O_{carb\text{-}w}$ values (Fig. 3.11) approaching the $\Delta^{18}O_{CO32-w}$ equilibrium (CO_3^{2-} oxygen isotope in equilibrium relative to water isotopes; Zeebe, 2007). This might be caused by either high calcite precipitation rates and/or precipitation at higher pH (e.g., Zeebe, 1999; Dietzel et al., 2009; Gabitov et al., 2012; Watkins et al., 2013, 2014; Li et al., 2020). However, based on the $\delta^{18}O$ data alone it is not possible to discriminate whether one or both of these factors influenced the $\Delta^{18}O_{carb\text{-}w}$ of these samples. In the following section we attempt to resolve this by the inclusion of boron isotopes which provide complementary information on the carbonate (bio)mineralisation processes.

On the other hand, calcite samples from hot spring and wetland sediments, microbialites, and travertines from the southern and western shores showed lower $\delta^{18}O_{carb}$ values than brine calcites,

although even lower values would be expected considering waters in these subenvironments present the lowest $\delta^{18}O_w$ values (Fig. 3.4a and 8a). This implies a stronger ^{18}O-enrichment relative to the parent waters compared to the brine calcites suggesting other controls on the $\delta^{18}O_{carb}$ signatures than the isotopic composition of the water. Calcites from the southern and western shore sub-environments, except one travertine from the western shore, offset towards higher $\Delta^{18}O_{carb\text{-}w}$ values (Fig. 3.11). This can be explained by isotopic disequilibrium due to kinetic fractionation effects under conditions of rapid CO_2 degassing (Kele et al., 2015; Daëron et al., 2019), which is in agreement with the high pCO_2 estimated for the parent waters (Table S2; Vignoni et al., 2023a). The loss of isotopically light CO_2 results in heavier DIC being taken up by calcite during precipitation (Watkins et al., 2014). Similar to the lake samples discussed above, for the western shore travertine the offset towards lower $\Delta^{18}O_{carb\text{-}w}$ values (Fig. 3.11) might be explained by high calcite precipitation rates and/or higher pH (e.g., Zeebe, 1999; Dietzel et al., 2009; Gabitov et al., 2012; Watkins et al., 2013, 2014; Li et al., 2020).

All calcites in the El Peinado basin show positive $\delta^{13}C_{carb}$ values evidencing a strong ^{13}C-enrichment and a progressively increasing $\delta^{13}C_{carb}$ trend from the southern and western shore sub-environments to the lake (Fig. 3.8a). This most likely results from the preferential loss of isotopically light CO_2 during strong degassing in the hydrothermally influenced environments and further degassing, albeit to a lesser extent as indicated by the pCO_2 decrease (Table S2; Vignoni et al., 2023a), during evaporation in the lake (Valero-Garcés et al., 1999; Affek and Zaarur, 2014; Mors et al., 2022). Preferential consumption of ^{12}C during photosynthesis might also lead to ^{13}C-enriched carbonates but the contribution of this process is difficult to constrain (Muller et al., 2022). Considering the strong influence of physical processes (i.e., CO_2 degassing and evaporation) in this system it is most likely that these exert the primary control on the $\delta^{13}C_{carb}$ of El Peinado calcites (Valero-Garcés et al., 1999, 2000, 2003), as also found in other saline lakes (e.g., Stiller et al., 1985; Golan et al., 2017; Beeler et al., 2020).

Some degree of secondary influences is apparent from the only moderate $\delta^{18}O_{carb}$ and $\delta^{13}C_{carb}$ correlation ($r = 0.64$; Fig. 3.8a), suggesting that their composition might be affected by other processes (e.g., water mixing) and/or variable rates of CO_2 degassing/evaporation considering the diversity of depositional environments within the basin. The main reason behind the lack of a stronger correlation, however, appears to be due to four outlying samples, which when excluded lead to an improved Pearson's correlation coefficient ($r = 0.84$, $n = 28$). Specifically, sample PEI19-HTS3-C-1 has both the highest $\delta^{13}C_{carb}$ and $\Delta^{18}O_{carb\text{-}w}$ which could be interpreted as stronger degassing at the hydrothermal water outlet (Fig. 3.8a and 11); samples PEI19-T-5 and PEI19-T-5_coating correspond to a travertine collected at the southernmost end of the system that had a very shallow water depth due to intense evaporation (Fig. 3.1c and 5c); and the sample PEI21-HTS1-C-2 corresponds to a carbonate covering the base and roots of

shrubs at the edge of the southern hydrothermal pool, where the ^{18}O-enrichment (highest $\Delta^{18}O_{carb\text{-}w}$ relative to the other southern samples; Fig. 3.11) could be enhanced by evaporation during capillary rise of water, as previously also suggested in Laguna Pastos Grandes (Bougeault et al., 2020). This highlights the control of the diversity of depositional environments on the $\delta^{18}O_{carb}$ and $\delta^{13}C_{carb}$ values, even over short distances, as has also been observed in other lake systems from the region (Buongiorno et al., 2019; Bougeault et al., 2020).

3.5.3.3. Controls on the $\delta^{11}B_{carb}$ composition

The $\delta^{11}B_{carb}$ values fall into different groups when compared to the predicted ambient $\delta^{11}B_4$ (Fig. 3.12), enabling us to distinguish precipitation processes linked to in situ pH change from those driven by other secondary factors. When the incorporation of the tetrahedral $B(OH)_4^-$ is controlled by the water pH, the $\delta^{11}B_{carb}$ should reflect the water $\delta^{11}B_4$ composition (as indicated by the 1:1 line in Fig. 3.12). While our $\delta^{11}B_{carb}$ values fall around the 1:1 line, they exhibit offsets. The positive $\delta^{11}B_{carb}$ offset (of on average 3.9‰) observed in the western shore hot spring and southern shore samples can be explained by elevated pH in the mineralisation microenvironment. The calculated $\delta^{11}B_{carb}$-derived pH (Eq. 7) gives values between 7.9 and 8.6 (Table S5), which is higher than the bulk water pH (between 5.1 and 6.5; Table S1; Vignoni et al., 2023a). Interestingly, these samples formed in waters undersaturated with respect to calcite (SI < 0; Table S2; Vignoni et al., 2023a). Photosynthetically-driven elevation of in situ pH by the thriving microorganism communities thus appears responsible for driving carbonate precipitation in these environments. Likewise, calcite from the western shore microbialites showed a positive offset, albeit of a lower magnitude (1.4‰ higher than the expected $\delta^{11}B_4$) possibly because of the SI > 0 in these waters, suggesting minor elevation of in situ pH at precipitation (Fig. 3.12; Table S2 and S5; Vignoni et al., 2023a).

Calcites from one of the short cores from Laguna del Peinado recorded $\delta^{11}B_{carb}$ values on average 4.5‰ lower than that of the predicted $\delta^{11}B_4$ (Fig. 3.12). A potential bias could result from contamination with clays that preferentially adsorb the relatively lighter ^{10}B (Palmer et al., 1987; Vengosh et al., 1991), which can be traced by elevated Al/Ca and B/Ca content. However, no clay minerals were identified by XRD or SEM and elevated Al/Ca and B/Ca in these samples did not translate into systematically lower $\delta^{11}B_{carb}$ values (Fig. S5, Table S4; Vignoni et al., 2023a), suggesting that the observed values most likely reflect real trends. Such relatively light $\delta^{11}B$ values have been also reported for amorphous silica crust and diatom-rich suspended sediment in a geothermal system in the Indian Himalayas (Steller et al., 2019) as well as marine biogenic silica (Ishikawa and Nakamura, 1993). This is thought to be driven by the substitution of the relatively light $^{10}B(OH)_4^-$ for silicate in tetrahedral sites in the diatom opal (Ishikawa and Nakamura, 1993; Steller et al., 2019) with an additional negative isotopic fractionation (i.e., towards ^{11}B-depleted values) taking place during incorporation (Donald et al., 2020). Contrary to carbonates, a significant

negative correlation has been observed between $\delta^{11}B$ in diatoms and pH (Donald et al., 2020). The low offset of $\delta^{11}B_{carb}$ values compared to the $\delta^{11}B_4$ in these waters could potentially result from the leaching of ^{10}B from diatoms within the microenvironment of carbonate precipitation (e.g., Hong et al., 2022) given the high abundance of diatoms in the sediment and travertines structure.

Calcites from Laguna Turquesa, the southeastern shore of Laguna del Peinado, and a travertine from the west coast, show a range of plausible $\delta^{11}B_4$ values which are largely biased towards lower than expected $\delta^{11}B_4$ at the measured in situ pH (Fig. 3.12; Table S6; Vignoni et al., 2023a). Given that at the measured pH the model indicated BA was higher than the measured TA (Table S6; Vignoni et al., 2023a), a lower pH for these water samples is plausible due to the challenges associated with measuring this parameter accurately in high ionic strength solutions (e.g., Bates, 1974; Covington and Ferra, 1994; Golan et al., 2014). Partially, this offset can be reconciled when $\delta^{11}B_4$ is calculated using the sit.dat instead of pitzer.dat (Fig. S4; Table S7; Vignoni et al., 2023a). Alternatively, a potential bias towards lower $\delta^{11}B_{carb}$ values could result from the influence of ^{11}B-depleted diatoms in the precipitation microenvironment or higher precipitation rates that increase the incorporation of $^{10}B(OH)_4^-$ into calcite as observed by Farmer et al. (2019). High precipitation rates are particularly likely in these hypersaline waters and would also explain the deviation from the expected oxygen isotopic equilibrium observed for these samples (Fig. 3.11).

3.5.4. Implications for interpreting geochemical signatures of lacustrine carbonates

Our comprehensive dataset of paired water-carbonate chemistry illuminates some of the key controls on the elemental and isotopic signatures of calcites forming in natural hypersaline and hydrothermal environments. These results enable us to elaborate on the potentials and limitations of lacustrine carbonates in Andean lake systems and similar environments as recorders of past environmental and hydroclimatic changes.

The high $\delta^{18}O_{carb}$ values from calcite deposited at the lake bottom suggest precipitation under isotopic equilibrium conditions and reflect the water evaporitic enrichment. However, the $\delta^{18}O_{carb}$ signatures in lake sediment records might be biased by the influence of other factors on $\delta^{18}O_w$, such as mixing with waters of different composition (e.g., thermal waters, groundwater), warning against a simplistic interpretation of $\delta^{18}O_{carb}$ as an exclusive indicator of evaporation (Valero-Garcés et al., 2000, 2001). In contrast, carbonates from the hydrothermal environments are formed at isotopic disequilibrium conditions between water and the DIC and thus are not suitable as a hydroclimate proxy. Lake $\delta^{13}C_{carb}$ signatures in such environments may be of limited use as a proxy because ^{13}C-enrichment could either reflect the evaporitic enrichment of the water DIC resulting from evaporation induced-CO_2 degassing and/or photosynthesis (Valero-Garcés et al., 1999; Beeler et al., 2020; Muller et al., 2022). Even so,

covariation of $\delta^{18}O_{carb}$ and $\delta^{13}C_{carb}$ are common in closed-basin lakes and considered to reflect evaporation, with the decoupling of this trend usually interpreted as changes in the basin hydrology, lake productivity, or changes in the DIC (Talbot, 1990; Li and Ku, 1997; Valero-Garcés et al., 1999, 2000, 2003). The oxygen and carbon isotope values of carbonates, however, if carefully interpreted could shed light on some of the pathways involved in the formation of the carbonates in the past and thus the processes operating in the basin.

The analysis of $\delta^{11}B_{carb}$ in lacustrine calcites provides a useful new tool for extending multiproxy geochemical approaches. Further information on the composition of the lake water, and hence the source rocks with which it interacted, as well as evaporitic trends can be obtained. Moreover, it also provides useful insights into the conditions in the precipitation microenvironment, such as pH changes caused by microbial metabolism.

Our results show that Na/Ca, Li/Ca, and B/Ca can provide information on water salinity. Na/Ca and Li/Ca ratios, however, could be biased by high calcite precipitation rates. The Mg/Ca content gives information on the Mg/Ca ratio of water, which, in hypersaline systems, can give insights into the degree of brine evolution as Ca^{2+} is consumed in mineral precipitation (Eugster, 1980). It may also indicate fluctuations in the input of high Mg waters, such as the southern shore hot springs, and weathering of Mg-rich lithologies (Deocampo, 2010).

3.6. Conclusions

The present study contributes to the understanding of the various processes that drive modern carbonate precipitation in lacustrine environments of the Altiplano-Puna Plateau and influence their geochemical signatures. The hypersaline El Peinado lacustrine system can be considered a type locality to study the complex interactions of evaporation, hydrothermal activity, and biological influences on carbonate formation in an active tectonic and volcanic setting. The integration of multi-proxy datasets is critical for robust interpretations and revealed the following:

1) The hydrothermal waters are undersaturated with respect to $CaCO_3$, but CO_2 degassing and biological activity produce a shift in the carbonate equilibrium and increase pH, favouring carbonate precipitation.
2) In the hypersaline lake system, carbonate precipitation is driven by high evaporation rates that increase $CaCO_3$ saturation state, as well as CO_2 degassing and biological activity depending on the location within the lake basin.
3) Microbial communities and diatoms influence carbonate precipitation by modifying the microenvironment geochemistry (pH, ions availability) and providing nucleation sites.

4) Li/Ca, B/Ca, and Na/Ca values reflect water salinity due to evaporative concentration. The Mg/Ca values record the Mg/Ca of the parent waters and, combined with the interpretation of other proxies, could serve as an indicator of the evolution of the brine or variations in the input of Mg-rich waters.
5) The $\delta^{18}O_{carb}$ signatures of modern lacustrine calcites largely reflect the strong evaporation and residence time of the waters, and to some extent likely also the high carbonate precipitation rates, whereas $\delta^{18}O_{carb}$ values of calcites forming in hot springs are dominated by disequilibrium effects from CO_2 degassing.
6) Lacustrine $\delta^{11}B_{carb}$ signatures are influenced by the $\delta^{11}B_w$, the pH of the water from which they precipitated, the pH in the precipitation microenvironment and thus provide insights into the carbonate (bio)mineralisation processes as well as the water source.

Our findings contribute to the development of proxies for these depositional environments, which is essential for the interpretation of the geochemical signatures of the different carbonates in the geological record.

Data Availability

Research data has been supplied via a repository: https://doi.org/10.5880/GFZ.4.3.2023.004.

Acknowledgements

This research was funded by the Deutsche Forschungsgemeinschaft (DFG) and the Federal State of Brandenburg under the auspices of the International Research Training Group IGK2018 “SuRfAce processes, TEctonics and Georesources: The Andean foreland basin of Argentina” (STRATEGy DFG 373/34-1), and by the GFZ German Research Centre for Geosciences who provided financial support for fieldwork.

This research was also carried out in the framework of the following Argentinean research projects: Agencia Nacional de Promoción Científica y Tecnológica (PICT-2019-01336), CONICET (PUE 2017-22920170100027CO and GII StRATEGy 163-A 1.1) and SECTER - Universidad Nacional de Jujuy (SeCTER-E/G011 and E/1001/-Integrar). H. Jurikova acknowledges funding from the DFG (Grant no. TJ 66/2-1), and both H.J. and J.W.B. Rae acknowledge funding from the European Research Council under the European Union’s Horizon 2020 research and innovation program (grant agreement 805246). We acknowledge the Secretaría de Estado del Ambiente y Desarrollo Sustentable and Dirección Provincial de Biodiversidad from the Gobierno de la Provincia de Catamarca (Argentina) for granting us the working permits, and Comunidad Coya Atacameña de Antofalla for supervising the fieldwork. We want to thank S. Vazquez and P. Martin for their invaluable help with the logistics and organisation of fieldwork in a remote and difficult

terrain. We are thankful to B. Brademann and E. Schnabel from the GFZ, Potsdam for their assistance with sample preparation and measurements. We further thank the associate editor Adrian Immenhauser and the two anonymous reviewers for their constructive comments and suggestions to improve this manuscript. We deeply regret the passing of our dear colleague Dr V. Liebetrau (from GEOMAR, Kiel) during the preparation of this manuscript, whose contributions to sample analyses, data interpretation and early versions of the text were invaluable.

References

Affek, H.P., Zaarur, S., 2014. Kinetic isotope effect in CO2 degassing: Insight from clumped and oxygen isotopes in laboratory precipitation experiments. Geochim. Cosmochim. Acta 143, 319–330.

Allmendinger, R.W., Jordan, T.E., Kay, S.M., Isacks, B. L., 1997. The evolution of the Altiplano-Puna Plateau of the Central Andes. Annu. Rev. Earth Planet. Sci. 25, 139–174.

Apolinarska, K., Pleskot, K., Pełechata, A., Migdałek, M., Pełechaty, M., 2021. Seasonal deposition of authigenic calcite out of isotopic equilibrium with DIC and water, and implications for paleolimnological studies. J. Paleolimnol. 66, 41–53.

Appelo, C.A.J., Parkhurst, D.L., Post, V.E.A., 2014. Equations for calculating hydrogeochemical reactions of minerals and gases such as CO2 at high pressures and temperatures. Geochim. Cosmochim. Acta 125, 49–67.

Arp, G., Reimer, A., Reitner, J., 2001. Photosynthesis-induced biofilm calcification and calcium concentrations in phanerozoic oceans. Science 292, 1701–1704.

Bates, R.G., 1974. Determination of pH: Theory and practice. 2nd ed., Wiley.

Beeler, S.R., Gomez, F.J., Bradley, A.S., 2020. Controls of extreme isotopic enrichment in modern microbialites and associated abiogenic carbonates. Geochim. Cosmochim. Acta 269, 136–149.

Bianchi, M., Heit, B., Jakovlev, A., Yuan, X., Kay, S.M., Sandvol, E., Alonso, R.N., Coira, B., Brown, L., Kind, R., Comte, D., 2013. Teleseismic tomography of the southern Puna plateau in Argentina and adjacent regions. Tectonophysics 586, 65–83.

Boschetti, T., Cifuentes, J., Iacumin, P., Selmo, E., 2019. Local meteoric water line of northern Chile (18° S-30° S): An application of error-in-variables regression to the oxygen and hydrogen stable isotope ratio of precipitation. Water 11, 791.

Bougeault, C., Durlet, C., Vennin, E., Muller, E., Ader, M., Ghaleb, B., Gérard, E., Virgone, A., Gaucher, E.C., 2020. Variability of Carbonate Isotope Signatures in a Hydrothermally Influenced System: Insights from the Pastos Grandes Caldera (Bolivia). Minerals 10, 989.

Bougeault, C., Vennin, E., Durlet, C., Muller, E., Mercuzot, M., Chavez, M., Gérard, E., Ader, M., Virgone, A., Gaucher, E.C., 2019. Biotic–Abiotic Influences on Modern Ca–Si-Rich Hydrothermal Spring Mounds of the Pastos Grandes Volcanic Caldera (Bolivia). Minerals 9, 380.

Boutt, D.F., Corenthal, L.G., Moran, B.J., Munk, L., Hynek, S.A., 2021. Imbalance in the modern hydrologic budget of topographic catchments along the western slope of the Andes (21–25°S): implications for groundwater recharge assessment. Hydrogeol. J. 29, 985–1007.

Buongiorno, J., Gomez, F.J., Fike, D.A., Kah, L.C., 2019. Mineralized microbialites as archives of environmental evolution, Laguna Negra, Catamarca Province, Argentina. Geobiology 17, 199–222.

Castino, F., Bookhagen, B., Strecker, M.R., 2017. Rainfall variability and trends of the past six decades (1950–2014) in the subtropical NW Argentine Andes. Clim. Dyn. 48, 1049–1067.

Chiodi, A., Tassi, F., Báez, W., Filipovich, R., Bustos, E., Glok Galli, M., Suzaño, N., Ahumada, M.F., Viramonte, J.G., Giordano, G., Pecoraino, G., Vaselli, O., 2019. Preliminary conceptual model of the

Cerro Blanco caldera-hosted geothermal system (Southern Puna, Argentina): Inferences from geochemical investigations. J. South Am. Earth Sci. 94, 102213.
Coplen, T.B., 2007. Calibration of the calcite-water oxygen-isotope geothermometer at Devils Hole, Nevada, a natural laboratory. Geochim. Cosmochim. Acta 71, 3948–3957.
Covington, A.K., Ferra, M.I.A., 1994. A pitzer mixed electrolyte solution theory approach to assignment of pH to standard buffer solutions. J. Solution Chem. 23, 1–10.
Craig, H., 1961. Isotopic variations in meteoric waters. Science. 133, 1702–1703.
Daëron, M., Drysdale, R.N., Peral, M., Huyghe, D., Blamart, D., Coplen, T.B., Lartaud, F., Zanchetta, G., 2019. Most Earth-surface calcites precipitate out of isotopic equilibrium. Nat. Commun. 10, 429.
Day, C.C., Henderson, G.M., 2013. Controls on trace-element partitioning in cave-analogue calcite. Geochim. Cosmochim. Acta 120, 612–627.
Della Vedova, M., Villafañe, P.G., Cónsole-Gonella, C., Bahniuk Rumbelsperger, A., Fadel Cury, L., Horta, L.R., Farías, M.E., 2022. Disentangling microstructure and environmental conditions in high-altitude Andean microbialite systems (Catamarca, Argentine Puna). Environ. Microbiol. Rep. 15, 92–108.
Deocampo, D.M., 2010. The Geochemistry of Continental Carbonates. In: Alonso-Zarza, A.M., Tanner, L.H. (Eds.), Carbonates in Continental Settings: Geochemistry, Diagenesis and Applications, Developments in Sedimentology. Elsevier, Amsterdam, pp. 1–59.
Dickson, A.G., 1990. Thermodynamics of the Dissociation of Boric Acid in Potassium Chloride Solutions from 273.15 to 318.15 K. J. Chem. Eng. Data 35, 253–257.
Dietzel, M., Tang, J., Leis, A., Köhler, S.J., 2009. Oxygen isotopic fractionation during inorganic calcite precipitation: effects of temperature, precipitation rate and pH. Chem. Geol. 268, 107–115.
Donald, H.K., Foster G.L., Fröhberg, N., Swann, G.E.A., Poulton, A.J., Moore, C.M., Humphreys, M.P., 2020. The pH dependency of the boron isotopic composition of diatom opal (Thalassiosira weissflogii). Biogeosciences 17, 2825–2837.
Dupraz, C., Reid, R.P., Braissant, O., Decho, A.W., Norman, R.S., Visscher, P.T., 2009. Processes of carbonate precipitation in modern microbial mats. Earth-Science Rev. 96, 141–162.
Eugster, H.P., 1980. Geochemistry of evaporitic lacustrine deposits. Annu. Rev. Earth Planet. Sci. 8, 35–63.
Farías, M.E., Saona Acuña, L.A., 2020. Modern Microbial Mats and Endoevaporite System in Andean Lakes: A General Approach. In: Farías, M.E. (Ed.), Microbial Ecosystems in Central Andes Extreme Environments. Springer, Cham, pp. 21–33.
Farías, M.E., Villafañe, P.G., Lencina, A.I., 2020. Integral Prospection of Andean Microbial Ecosystem Project. In: Farías, M.E. (Ed.), Microbial Ecosystems in Central Andes Extreme Environments. Springer, Cham, pp. 245–260.
Farmer, J.R., Branson, O., Uchikawa, J., Penman, D.E., Hönisch, B., Zeebe, R.E., 2019. Boric acid and borate incorporation in inorganic calcite inferred from B/Ca, boron isotopes and surface kinetic modeling. Geochim. Cosmochim. Acta 244, 229–247.
Frau, D., Moran, B.J., Arengo, F., Marconi, P., Battauz, Y., Mora, C., Manzo, R., Mayora, G., Boutt, D.F., 2021. Hydroclimatological Patterns and Limnological Characteristics of Unique Wetland Systems on the Argentine High Andean Plateau. Hydrology 8, 164.
Füger, A., Konrad, F., Leis, A., Dietzel, M., Mavromatis, V., 2019. Effect of growth rate and pH on lithium incorporation in calcite. Geochim. Cosmochim. Acta 248, 14–24.
Gabitov, R.I., Sadekov, A., Leinweber, A., 2014. Crystal growth rate effect on Mg/Ca and Sr/Ca partitioning between calcite and fluid: An in situ approach. Chem. Geol. 367, 70–82.
Gabitov, R.I., Watson, E.B., Sadekov, A., 2012. Oxygen isotope fractionation between calcite and fluid as a function of growth rate and temperature: An in situ study. Chem. Geol. 306–307, 92–102.
Garreaud, R., Vuille, M., Clement, A.C., 2003. The climate of the Altiplano: Observed current conditions and mechanisms of past changes. Palaeogeogr. Palaeoclimatol. Palaeoecol. 194, 5–22.
Garreaud, R.D., Vuille, M., Compagnucci, R., Marengo, J., 2009. Present-day South American climate.

Palaeogeogr. Palaeoclimatol. Palaeoecol. 281, 180–195.
Gascoyne, M., 1983. Trace-element partition coefficients in the calcite-water system and their paleoclimatic significance in cave studies. J. Hydrol. 61, 213–222.
Gayo, E.M., Latorre, C., Jordan, T.E., Nester, P.L., Estay, S.A., Ojeda, K.F., Santoro, C.M., 2012. Late Quaternary hydrological and ecological changes in the hyperarid core of the northern Atacama Desert (~21°S). Earth-Science Rev. 113, 120–140.
Geske, A., Zorlu, J., Richter, D.K., Buhl, D., Niedermayr, A., Immenhauser, A., 2012. Impact of diagenesis and low grade metamorphosis on isotope (δ26Mg, δ13C, δ18O and 87Sr/86Sr) and elemental (Ca, Mg, Mn, Fe and Sr) signatures of Triassic sabkha dolomites. Chem. Geol. 332–333, 45–64.
Giggenbach, W.F., 1988. Geothermal solute equilibria. Derivation of Na-K-Mg-Ca geoindicators. Geochim. Cosmochim. Acta 52, 2749–2765.
Godfrey, L., Jordan, T., Lowenstein, T., Alonso, R., 2003. Stable isotope constraints on the transport of water to the Andes between 22° and 26°S during the last glacial cycle. Palaeogeogr. Palaeoclimatol. Palaeoecol. 194, 299–317.
Golan, R., Gavrieli, I., Ganor, J., Lazar, B., 2016. Controls on the pH of hyper-saline lakes - A lesson from the Dead Sea. Earth Planet. Sci. Lett. 434, 289–297.
Golan, R., Gavrieli, I., Lazar, B., Ganor, J., 2014. The determination of pH in hypersaline lakes with a conventional combination glass electrode. Limnol. Oceanogr. Methods 12, 810–815.
Golan, R., Lazar, B., Wurgaft, E., Lensky, N., Ganor, J., Gavrieli I., 2017. Continuous CO 2 escape from the hypersaline Dead Sea caused by aragonite precipitation. Geochim. Cosmochim. Acta 207, 43–56.
Gomez, F.J., Boidi, F.J., Mlewski, C., Gérard, E., 2020. The Carbonate System in Hypersaline Lakes: The Case of Laguna Negra (in the Puna Region of Catamarca, Argentina). In: Farías, M.E. (Ed.), Microbial Ecosystems in Central Andes Extreme Environments. Springer, Cham, pp. 231–242.
Gomez, F.J., Kah, L.C., Bartley, J.K., Astini, R.A., 2014. Microbialites in a high-altitude Andean lake: Multiple controls on carbonate precipitation and lamina accretion. Palaios 29, 233–249.
Gomez, F.J., Mlewski, C., Boidi, F.J., Farías, M.E., Gérard, E., 2018. Calcium carbonate precipitation in diatom-rich microbial mats: The laguna negra hypersaline lake, catamarca, Argentina. J. Sediment. Res. 88, 727–742.
Gonfiantini, R., Roche, M.A., Olivry, J.C., Fontes, J.C., Zuppi, G.M., 2001. The altitude effect on the isotopic composition of tropical rains. Chem. Geol. 181, 147–167.
Grosjean, M., Valero-Garcés, B.L., Geyh, M.A., Messerli, B., Schotterer, U., Schreier, H., Kelts, K., 1997. Mid- and late-Holocene limnogeology of Laguna del Negro Francisco, northern Chile, and its palaeoclimatic implications. Holocene 7, 151–159.
Grosse, P., Guzmán, S.R., Nauret, F., Orihashi, Y., Sumino, H., 2022. Central vs. lateral growth and evolution of the < 100 ka Peinado composite volcano, southern Central Volcanic Zone of the Andes. J. Volcanol. Geotherm. Res. 425, 107532.
Grosse, P., Ochi Ramacciotti, M.L., Escalante Fochi, F., Guzmán, S., Orihashi, Y., Sumino, H., 2020. Geomorphology, morphometry, spatial distribution and ages of mafic monogenetic volcanoes of the Peinado and Incahuasi fields, southernmost Central Volcanic Zone of the Andes. J. Volcanol. Geotherm. Res. 401, 106966.
Hemming, N.G., Hanson, G.N., 1992. Boron isotopic composition and concentration in modern marine carbonates. Geochim. Cosmochim. Acta 56, 537–543.
Hemming, N.G., Reeder, R.J., Hanson, G.N., 1995. Mineral-fluid partitioning and isotopic fractionation of boron in synthetic calcium carbonate. Geochim. Cosmochim. Acta 59, 371–379.
Henehan, M.J., Klein Gebbinck, C.D., Wyman, J.V.B., Hain, M.P., Rae, J.W.B., Hönisch, B., Foster, G.L., Kim, S.-T., 2022. No ion is an island: Multiple ions influence boron incorporation into CaCO3. Geochim. Cosmochim. Acta 318, 510–530.
Hoefs, J., 2015. Stable Isotope Geochemistry, seventh ed. Springer, Cham.

Hong, W.L., Lepland, A., Kirsimäe, K., Crémière, A., Rae, J.W.B., 2022. Boron concentrations and isotopic compositions in methane-derived authigenic carbonates: Constraints and limitations in reconstructing formation conditions. Earth Planet. Sci. Lett. 579, 117337.

Huffman, G.J., Bolvin, D.T., Nelkin, E.J., Wolff, D.B., Adler, R.F., Gu, G., Hong, Y., Bowman, K.P., Stocker, E.F., 2007. The TRMM Multisatellite Precipitation Analysis (TMPA): Quasi-Global, Multiyear, Combined-Sensor Precipitation Estimates at Fine Scales. J. Hydrometeorol. 8, 38–55.

Immenhauser, A., Kenter, J.A.M., Ganssen, G., Bahamonde, J.R., Van Vliet, A., Saher, M.H., 2002. Origin and Significance of Isotope Shifts in Pennsylvanian Carbonates (Asturias, NW Spain). J. Sediment. Res. 72, 82–94.

Ishikawa, M., Ichikuni, M., 1984. Uptake of sodium and potassium by calcite. Chem. Geol. 42, 137–146.

Ishikawa, T., Nakamura, E., 1993. Boron isotope systematics of marine sediments. Earth Planet. Sci. Lett. 117, 567–580.

Jones, B., Peng, X., 2016. Mineralogical, crystallographic, and isotopic constraints on the precipitation of aragonite and calcite at Shiqiang and other hot springs in Yunnan Province, China. Sediment. Geol. 345, 103–125.

Jurikova, H., Ippach, M., Liebetrau, V., Gutjahr, M., Krause, S., Büsse, S., Gorb, S.N., Henkel, D., Hiebenthal, C., Schmidt, M., Leipe, T., Laudien, J., Eisenhauer, A., 2020. Incorporation of minor and trace elements into cultured brachiopods: Implications for proxy application with new insights from a biomineralisation model. Geochim. Cosmochim. Acta 286, 418–440.

Jurikova, H., Liebetrau, V., Gutjahr, M., Rollion-Bard, C., Hu, M.Y., Krause, S., Henkel, D., Hiebenthal, C., Schmidt, M., Laudien, J., Eisenhauer, A., 2019. Boron isotope systematics of cultured brachiopods: Response to acidification, vital effects and implications for palaeo-pH reconstruction. Geochim. Cosmochim. Acta 248, 370–386.

Jurikova, H., Ring, S.J., Henehan, M.J., Neugebauer, I., Schröder, B., Müller, D., Schwab, M.J., Tjallingii, R., Brauer, A., Blanchet, C., 2023. Boron geochemistry reveals the evolution of Dead Sea brines. Earth Planet. Sci. Lett. 622, 118403.

Kasemann, S.A., Meixner, A., Erzinger, J., Viramonte, J.G., Alonso, R.N., Franz, G., 2004. Boron isotope composition of geothermal fluids and borate minerals from salar deposits (central Andes/NW Argentina). J. South Am. Earth Sci. 16, 685–697.

Katz, A., 1973. The interaction of magnesium with calcite during crystal growth at 25-90°C and one atmosphere. Geochim. Cosmochim. Acta 37, 1563–1586.

Kay, S.M., Coira, B.L., Caffe, P.J., Chen, C.H., 2010. Regional chemical diversity, crustal and mantle sources and evolution of central Andean Puna plateau ignimbrites. J. Volcanol. Geotherm. Res. 198, 81–111.

Kele, S., Breitenbach, S.F.M., Capezzuoli, E., Meckler, A.N., Ziegler, M., Millan, I.M., Kluge, T., Deák, J., Hanselmann, K., John, C.M., Yan, H., Liu, Z., Bernasconi, S.M., 2015. Temperature dependence of oxygen- and clumped isotope fractionation in carbonates: A study of travertines and tufas in the 6-95°C temperature range. Geochim. Cosmochim. Acta 168, 172–192.

Kele, S., Özkul, M., Fórizs, I., Gökgöz, A., Baykara, M.O., Alçiçek, M.C., Németh, T., 2011. Stable isotope geochemical study of Pamukkale travertines: New evidences of low-temperature non-equilibrium calcite-water fractionation. Sediment. Geol. 238, 191–212.

Kim, S.T., O'Neil, J.R., 1997. Equilibrium and nonequilibrium oxygen isotope effects in synthetic carbonates. Geochim. Cosmochim. Acta 61, 3461–3475.

Kitano, Y., Okumura, M., Idogaki, M., 1978. Coprecipitation of borate-boron with calcium carbonate. Geochem. J. 12, 183–189.

Klochko, K., Kaufman, A.J., Yao, W., Byrne, R.H., Tossell, J.A., 2006. Experimental measurement of boron isotope fractionation in seawater. Earth Planet. Sci. Lett. 248, 276–285.

Latorre, C., Betancourt, J.L., Arroyo, M.T.K., 2006. Late Quaternary vegetation and climate history of a perennial river canyon in the Río Salado basin (22°S) of Northern Chile. Quat. Res. 65, 450–466.

Leng,M.J., Marshall, J. D., 2004. Palaeoclimate interpretation of stable isotope data from lake sediment archives. Quat. Sci. Rev. 23, 811–831.

Li, H., Liu, X., Tripati, A., Feng, S., Elliott, B., Whicker, C., Arnold, A., Kelley, A.M., 2020. Factors controlling the oxygen isotopic composition of lacustrine authigenic carbonates in Western China: implications for paleoclimate reconstructions. Sci. Rep. 10, 1–17.

Li, H.C., Ku, T.L., 1997. δ13C–δ18C covariance as a paleohydrological indicator for closed-basin lakes. Palaeogeogr. Palaeoclimatol. Palaeoecol. 133, 69–80.

Marriott, C.S., Henderson, G.M., Crompton, R., Staubwasser, M., Shaw, S., 2004. Effect of mineralogy, salinity, and temperature on Li/Ca and Li isotope composition of calcium carbonate. Chem. Geol. 212, 5–15.

Mavromatis, V., Montouillout, V., Noireaux, J., Gaillardet, J., Schott, J., 2015. Characterization of boron incorporation and speciation in calcite and aragonite from co-precipitation experiments under controlled pH, temperature and precipitation rate. Geochim. Cosmochim. Acta 150, 299–313.

McCormack, J., Nehrke, G., Jöns, N., Immenhauser, A., Kwiecien, O., 2019. Refining the interpretation of lacustrine carbonate isotope records: Implications of a mineralogy-specific Lake Van case study. Chem. Geol. 513, 167–183.

McGlue, M.M., Cohen, A.S., Ellis, G.S., Kowler, A.L., 2013. Late Quaternary stratigraphy, sedimentology and geochemistry of an underfilled lake basin in the Puna plateau (northwest Argentina). Basin Res. 25, 638–658.

Mitnick, E.H., 2018. Stable isotope fractionation and trace element partitioning in marine, terrestrial, and laboratory-synthesized carbonates. P.h. D thesis, University of California, Berkeley.

Mlewski, E.C., Pisapia, C., Gomez, F., Lecourt, L., Rueda, E.S., Benzerara, K., Ménez, B., Borensztajn, S., Jamme, F., Réfrégiers, M., Gérard, E., 2018. Characterization of pustular mats and related Rivularia-rich laminations in oncoids from the Laguna Negra lake (Argentina). Front. Microbiol. 9, 1–23.

Morales, M.S., Carilla, J., Grau, H.R., Villalba, R., 2015. Multi-century lake area changes in the Southern Altiplano: a tree-ring-based reconstruction. Clim. Past 11, 1139–1152.

Moran, B.J., Boutt, D.F., Munk, L.A., 2019. Stable and Radioisotope Systematics Reveal Fossil Water as Fundamental Characteristic of Arid Orogenic-Scale Groundwater Systems. Water Resour. Res. 55, 11295–11315.

Morris, R.V., Ruff, S.W., Gellert, R., Ming, D.W., Arvidson, R.E., Clark, B.C., Golden, D.C., Siebach, K., Klingelhöfer, G., Schröder, C., Fleischer, I., Yen, A.S., Squyres, S.W., 2010. Identification of Carbonate-Rich Outcrops on Mars by the Spirit Rover. Science 329, 421–424.

Mors, R.A., Gomez, F.J., Astini, R.A., Mlewski, E.C., Gérard, E., 2022. Physico-chemical and biological controls in a travertine system in the high Andes of northwestern Argentina. Sediment. Geol. 439, 106214.

Morse, J.W., Bender, M.L., 1990. Partition coefficients in calcite: Examination of factors influencing the validity of experimental results and their application to natural systems. Chem. Geol. 82, 265–277.

Mucci, A., Morse, J.W., 1983. The incorporation of Mg^{2+} and Sr^{2+} into calcite overgrowths: influences of growth rate and solution composition. Geochim. Cosmochim. Acta 47, 217–233.

Muller, E., Ader, M., Aloisi, G., Bougeault, C., Durlet, C., Vennin, E., Benzerara, K., Gaucher, E.C., Virgone, A., Chavez, M., Souquet, P., Gérard, E., 2022. Successive Modes of Carbonate Precipitation in Microbialites along the Hydrothermal Spring of La Salsa in Laguna Pastos Grandes (Bolivian Altiplano). Geosciences 12, 88.

Muller, E., Gaucher, E.C., Durlet, C., Moquet, J.S., Moreira, M., Rouchon, V., Louvat, P., Bardoux, G., Noirez, S., Bougeault, C., Vennin, E., Gérard, E., Chavez, M., Virgone, A., Ader, M., 2020. The origin of continental carbonates in Andean salars: A multi-tracer geochemical approach in Laguna Pastos Grandes (Bolivia). Geochim. Cosmochim. Acta 279, 220–237.

Nir, O., Vengosh, A., Harkness, J.S., Dwyer, G.S., Lahav, O., 2015. Direct measurement of the boron isotope

fractionation factor: Reducing the uncertainty in reconstructing ocean paleo-pH. Earth Planet. Sci. Lett. 414, 1–5.

Palmer, M.R., Spivack, A.J., Edmond, J.M., 1987. Temperature and pH controls over isotopic fractionation during adsorption of boron on marine clay. Geochim. Cosmochim. Acta 51, 2319–2323.

Parkhurst, D.L., Appelo, C.A.J., 2013. Description of Input and Examples for PHREEQC Version 3: a computer program for speciation, batch-reaction, one-dimensional transport, and inverse geochemical calculations. U.S. Geological Survey Techniques and Methods, book 6, chap. A43.

Peralta Arnold, Y., Cabassi, J., Tassi, F., Caffe, P.J., Vaselli, O., 2017. Fluid geochemistry of a deep-seated geothermal resource in the Puna plateau (Jujuy Province, Argentina). J. Volcanol. Geotherm. Res. 338, 121–134.

Piovano, E.L., Córdoba, F.E., Stutz, S., 2014. Limnogeology in Southern South America: An overview. Lat. Am. J. Sedimentol. Basin Anal. 21, 65–75.

Placzek, C., Quade, J., Betancourt, J.L., Patchett, P.J., Rech, J.A., Latorre, C., Matmon, A., Holmgren, C., English, N.B., 2009. Climate in the dry central andes over geologic, millennial, and interannual timescales. Ann. Missouri Bot. Gard. 96, 386–397.

Plummer, L.N., Parkhurst, D.L., Fleming, G.W., Dunkle, S.A., 1988. A computer program incorporating Pitzer's equations for calculation of geochemical reactions in brines. U.S. Geological Survey Water-Resources Investigations Report 88–4153.

Rimstidt, J.D., Balog, A., Webb, J., 1998. Distribution of trace elements between carbonate minerals and aqueous solutions. Geochim. Cosmochim. Acta 62, 1851–1863.

Rohrmann, A., Strecker, M.R., Bookhagen, B., Mulch A., Sachse, D., Pingel, H., Alonso, R.N., Schildgen, T.F., Montero, C., 2014. Can stable isotopes ride out the storms? The role of convection for water isotopes in models, records, and paleoaltimetry studies in the central Andes. Earth Planet. Sci. Lett. 407, 187–195.

Rosner, M., Erzinger, J., Franz, G., Trumbull, R.B., 2003. Slab-derived boron isotope signatures in arc volcanic rocks from the Central Andes and evidence for boron isotope fractionation during progressive slab dehydration. Geochemistry, Geophys. Geosystems 4, 9005.

Ryves, D.B., Leng, M.J., Barker, P.A., Snelling, A.M., Sloane, H.J., Arrowsmith, C., Tyler, J.J., Scott, D.R., Radbourne, A.D., Anderson, N.J., 2020. Understanding the transfer of contemporary temperature signals into lake sediments via paired oxygen isotope ratios in carbonates and diatom silica: Problems and potential. Chem. Geol. 552, 119705.

Santamans, C.D., Cordoba, F.E., Franco, M.G., Vignoni, P. , Lupo, L.C., 2021. Hydro-climatological variability in Lagunas de Vilama System, Argentinean Altiplano-Puna Plateau, Southern Tropical Andes (22° S), and its response to large-scale climate forcings. Sci. Total Environ. 767, 144926.

Shiraishi, F., Hanzawa, Y., Nakamura, Y., Eno, Y., Morikawa, A., de Mattos, R.F., Asada, J., Cury, L.F., Bahniuk, A.M., 2022. Abiotic and biotic processes controlling travertine deposition: Insights from eight hot springs in Japan. Sedimentology 69, 592–623.

Shiraishi, F., Hanzawa, Y., Nakamura, Y., Eno, Y., Morikawa, A., de Mattos, R.F., Asada, J., Cury, L.F., Bahniuk, A.M., 2022. Abiotic and biotic processes controlling travertine deposition: Insights from eight hot springs in Japan ed. C. Arenas. Sedimentology 69, 592–623.

Steller, L.H., Nakamura, E., Ota, T., Sakaguchi, C., Sharma, M., Van Kranendonk, M.J., 2019. Boron Isotopes in the Puga Geothermal System, India, and Their Implications for the Habitat of Early Life. Astrobiology 19, 1459–1473.

Stewart, J.A., Christopher, S.J., Kucklick, J.R., Bordier, L., Chalk, T.B., Dapoigny, A., Douville, E., Foster, G.L., Gray, W.R., Greenop, R., Gutjahr, M., Hemsing, F., Henehan, M.J., Holdship, P., Hsieh, Y., Kolevica, A., Lin, Y., Mawbey, E.M., Rae, J. W.B., Robinson, L.F., Shuttleworth, R., You, C., Zhang, S., Day, R.D., 2020. NIST RM 8301 Boron Isotopes in Marine Carbonate (Simulated Coral and Foraminifera Solutions): Inter-laboratory δ 11 B and Trace Element Ratio Value Assignment. Geostand.

Geoanalytical Res. 45, 77–96.
Stiller, M., Rounick, J.S., Shasha, S., 1985. Extreme carbon-isotope enrichments in evaporating brines. Nature 316, 434–435.
Strecker, M.R., Alonso, R.N., Bookhagen, B., Carrapa, B., Hilley, G.E., Sobel, E.R., Trauth, M.H., 2007. Tectonics and climate of the southern central Andes. Annu. Rev. Earth Planet. Sci. 35, 747–787.
Talbot, M.R., 1990. A review of the palaeohydrological interpretation of carbon and oxygen isotopic ratios in primary lacustrine carbonates. Chem. Geol. Isot. Geosci. Sect. 80, 261–279.
Tanner, L.H., 2010. Continental Carbonates as Indicators of Paleoclimate. In: Alonso-Zarza, A.M., Tanner, L.H. (Eds.), Carbonates in Continental Settings: Geochemistry, Diagenesis and Applications, Developments in Sedimentology. Elsevier, Amsterdam, pp. 179–214.
Tremaine D. M., Froelich P. N. and Wang Y. (2011) Speleothem calcite farmed in situ: modern calibration of d18O and d13C paleoclimate proxies in a continuously-monitored natural cave system. Geochim. Cosmochim. Acta 75, 4929–4950.
Valero-Garcés, B.L., Arenas, C., Delgado-Huertas, A., 2001. Depositional environments of Quaternary lacustrine travertines and stromatolites from high-altitude Andean lakes, Northwestern Argentina. Can. J. Earth Sci. 38, 1263–1283.
Valero-Garcés, B.L., Delgado-Huertas, A., Navas, A., Edwards, L., Schwalb, A., Ratto, N., 2003. Patterns of regional hydrological variability in central-southern Altiplano (18°-26°S) lakes during the last 500 years. Palaeogeogr. Palaeoclimatol. Palaeoecol. 194, 319–338.
Valero-Garcés, B.L., Delgado-Huertas, A., Ratto, N., Navas, A., 1999. Large 13C enrichment in primary carbonates from Andean Altiplano lakes, northwest Argentina. Earth Planet. Sci. Lett. 171, 253–266.
Valero-Garcés, B., Delgado-Huertas, A., Ratto, N., Navas, A., Edwards, L., 2000. Paleohydrology of Andean saline lakes from sedimentological and isotopic records, Northwestern Argentina. J. Paleolimnol. 24, 343–359.
Vengosh, A., Starinsky, A., Kolodny, Y., Chivas, A.R., 1991. Boron isotope geochemistry as a tracer for the evolution of brines and associated hot springs from the Dead Sea, Israel. Geochim. Cosmochim. Acta 55, 1689–1695.
Vignale, F.A., Lencina, A.I., Stepanenko, T.M., Soria, M.N., Saona, L.A., Kurth, D., Guzmán, D., Foster, J.S., Poiré, D.G., Villafañe, P.G., Albarracín, V.H., Contreras, M., Farías, M.E., 2022. Lithifying and Non-Lithifying Microbial Ecosystems in the Wetlands and Salt Flats of the Central Andes. Microb. Ecol. 83, 1–17.
[dataset] Vignoni, P.A., Jurikova, H., Schröder, B., Tjallingii, R., Córdoba, F.E., Liebetrau, V., Lecomte, K.L., Pinkerneil, S., Grudzinska, I., Schleicher, A.M., Viotto, S.A., Santamans, C., Rae, J.W.B., Brauer, A., 2023a. A database of the elemental and isotopic composition of water and carbonates from a hypersaline Andean lake (Laguna del Peinado, Argentina). GFZ Data Services, v1. doi.org/10.5880/GFZ.4.3.2023.004.
Vignoni, P.A., Córdoba, F.E., Tjallingii, R., Santamans, C., Lupo, L.C., Brauer, A., 2023b. Spatial variability of the modern radiocarbon reservoir effect in the high-altitude lake Laguna del Peinado (Southern Puna Plateau, Argentina). Geochronology, 1–19.
Villafañe, P.G., Cónsole-Gonella, C., Cury, L.F., Farías, M.E., 2021. Short-term microbialite resurgence as indicator of ecological resilience against crises (Catamarca, Argentine Puna). Environ. Microbiol. Rep. 13, 659–667.
Villalba, R., Grosjean, M., Kiefer, T., 2009. Long-term multi-proxy climate reconstructions and dynamics in South America (LOTRED-SA): State of the art and perspectives. Palaeogeogr. Palaeoclimatol. Palaeoecol. 281, 175–179.
Ward, K.M., Delph, J.R., Zandt, G., Beck, S.L., Ducea, M.N., 2017. Magmatic evolution of a Cordilleran flare-up and its role in the creation of silicic crust. Sci. Rep. 7, 1–8.
Wassenburg, J.A., Riechelmann, S., Schröder-Ritzrau, A., Riechelmann, D.F.C., Richter, D.K., Immenhauser,

A., Terente, M., Constantin, S., Hachenberg, A., Hansen, M., Scholz D., 2020. Calcite Mg and Sr partition coefficients in cave environments: Implications for interpreting prior calcite precipitation in speleothems. Geochim. Cosmochim. Acta 269, 581–596.

Watkins, J.M., Hunt, J.D., Ryerson, F.J., DePaolo, D.J., 2014. The influence of temperature, pH, and growth rate on the δ18O composition of inorganically precipitated calcite. Earth Planet. Sci. Lett. 404, 332–343.

Watkins, J.M., Nielsen, L.C., Ryerson, F.J., DePaolo, D.J., 2013. The influence of kinetics on the oxygen isotope composition of calcium carbonate. Earth Planet. Sci. Lett. 375, 349–360.

Zeebe, R.E., 1999. An explanation of the effect of seawater carbonate concentration on foraminiferal oxygen isotopes. Geochim. Cosmochim. Acta 63, 2001–2007.

Zeebe, R.E., 2007. An expression for the overall oxygen isotope fractionation between the sum of dissolved inorganic carbon and water. Geochemistry, Geophys. Geosystems 8, Q09002.

Zeebe, R.E., Rae, J.W.B., 2020. Equilibria, kinetics, and boron isotope partitioning in the aqueous boric acid–hydrofluoric acid system. Chem. Geol. 550, 119693.

Zeebe, R.E., Wolf-Gladrow, D., 2001. CO2 in seawater: equilibrium, kinetics, isotopes. 1st ed., Elsevier.